J Neurophysiol 122: 691–706, 2019.
First published July 3, 2019; doi:10.1152/jn.00048.2019.

RESEARCH ARTICLE | *Sensory Processing*

Active membrane conductances and morphology of a collision detection neuron broaden its impedance profile and improve discrimination of input synchrony

Richard B. Dewell[1] and Fabrizio Gabbiani[1,2]

[1]*Department of Neuroscience, Baylor College of Medicine, Houston, Texas; and* [2]*Department of Electrical and Computer Engineering, Rice University, Houston, Texas*

Submitted 22 January 2019; accepted in final form 13 June 2019

Dewell RB, Gabbiani F. Active membrane conductances and morphology of a collision detection neuron broaden its impedance profile and improve discrimination of input synchrony. *J Neurophysiol* 122: 691–706, 2019. First published July 3, 2019; doi: 10.1152/jn.00048.2019.—How neurons filter and integrate their complex patterns of synaptic inputs is central to their role in neural information processing. Synaptic filtering and integration are shaped by the frequency-dependent neuronal membrane impedance. Using single and dual dendritic recordings in vivo, pharmacology, and computational modeling, we characterized the membrane impedance of a collision detection neuron in the grasshopper *Schistocerca americana*. This neuron, the lobula giant movement detector (LGMD), exhibits consistent impedance properties across frequencies and membrane potentials. Two common active conductances g_H and g_M, mediated respectively by hyperpolarization-activated cyclic nucleotide-gated (HCN) channels and by muscarine-sensitive M-type K^+ channels, promote broadband integration with high temporal precision over the LGMD's natural range of membrane potentials and synaptic input frequencies. Additionally, we found that a model based on the LGMD's branching morphology increased the gain and decreased the delay associated with the mapping of synaptic input currents to membrane potential. More generally, this was true for a wide range of model neuron morphologies, including those of neocortical pyramidal neurons and cerebellar Purkinje cells. These findings show the unexpected role played by two widespread active conductances and by dendritic morphology in shaping synaptic integration.

NEW & NOTEWORTHY Neuronal filtering and integration of synaptic input patterns depend on the electrochemical properties of dendrites. We used an identified collision detection neuron in grasshoppers to examine how its morphology and two conductances affect its membrane impedance in relation to the computations it performs. The neuronal properties examined are ubiquitous and therefore promote a general understanding of neuronal computations, including those in the human brain.

collision avoidance; dendritic processing; lobula giant movement detector; membrane impedance

INTRODUCTION

By the 1940s, neuroscientists had recognized that neuronal membranes exhibited a frequency-dependent impedance and had begun investigating which cellular mechanisms contributed to their resistance, capacitance, and inductance (Cole 1941). The capacitance of the membrane is determined by its lipid bilayer and its resistance by permeability to ion fluxes, but the inductance came from an unknown source. After the discovery of active conductances, it became clear that their kinetics produced a phenomenological inductance and that its properties could be investigated with Hodgkin and Huxley's equations (Mauro 1961; Mauro et al. 1970).

Membrane capacitance low-passes whereas inductance high-passes input currents. Their combination can thus result in band-pass filtering and resonance. In the decades since, researchers have learned a great deal about the role of active conductances in shaping the electrical properties of neurons and the influence of neuronal band-pass properties on rhythmic activity within neural networks (Das et al. 2017; Hutcheon and Yarom 2000; Wang 2010). In addition to generating neural rhythms, the membrane impedance shapes the integration properties of dendrites, influencing their ability to discriminate between patterns of synaptic inputs (Branco et al. 2010; Branco and Häusser 2011; Dembrow et al. 2015; Spruston 2008; Vaidya and Johnston 2013).

In a passive neuron, membrane potential (V_m) changes trail low-frequency stimuli with an increasing delay approaching the membrane time constant as frequency decreases toward zero. The differing delays for inputs of different frequencies may reduce the ability of neurons to determine their relative synaptic input arrival times. To prevent this, auditory neurons that precisely discriminate the timing of their synaptic inputs have small time constants (~0.3 ms), thereby minimizing the offset between input current and change in V_m (McGinley et al. 2012; Mikiel-Hunter et al. 2016; Remme et al. 2014).

Voltage-gated channels modify the membrane impedance through their time-varying conductances. The range of input frequencies affected depends on the channel kinetics. Noninactivating channels whose conductance decreases as V_m approaches their reversal potential produce negative feedback on changes in V_m and thus a phenomenological inductance. These channels have often been described as "resonant" (Das et al. 2017; Hu et al. 2009; Hutcheon and Yarom 2000; Narayanan and Johnston 2008; Rotstein and Nadim 2014). In the lobula giant movement detector (LGMD) two such inductive channels, hyperpolarization-acti-

Address for reprint requests and other correspondence: R. B. Dewell, Dept. of Neuroscience, Baylor College of Medicine, Houston, TX 77030 (e-mail: dewell@bcm.edu).

vated cyclic nucleotide-gated (HCN) and muscarine-sensitive (M) channels, produce the largest resting conductances, influencing the selectivity and timing of its responses (Dewell and Gabbiani 2018a, 2018b). The impedance profile of a neuron is also influenced by its dendritic morphology. An extended morphology causes dendritic compartmentalization, which increases the attenuation and lag of postsynaptic potentials traveling toward the spike initiation zone (SIZ) but simultaneously enhances local coincidence detection and nonlinear processing (Häusser and Mel 2003; London and Häusser 2005). Dendritic branching and tapering could optimize synaptic integration by increasing the spatial homogeneity of postsynaptic potentials after propagation to the site of spike initiation (Cuntz et al. 2007). Additionally, the dendritic morphology of pyramidal and Purkinje neurons could favor their response to inputs of certain frequencies, thus promoting neuronal resonance (Dhupia et al. 2015; Ostojic et al. 2015).

We have chosen to explore the membrane impedance's determinants and its influence on neural processing in the LGMD (O'Shea and Williams 1974), an identified neuron in locusts that selectively responds to visual stimuli mimicking impending collision (Rind and Simmons 1992; Schlotterer 1977). The LGMD's stimulus selectivity arises from the precise spatiotemporal patterning of synaptic inputs (Jones and Gabbiani 2010; Peron et al. 2007; Zhu and Gabbiani 2016) and complex dendritic computations, including filtering by active conductances such as sodium, low voltage-activated calcium, calcium-dependent potassium, inactivating potassium, HCN, and M channels (Dewell and Gabbiani 2018a, 2018b; Gabbiani et al. 2002; Peron and Gabbiani 2009). Different aspects of the LGMD's firing patterns, including burst firing, have been tied to the generation of escape behaviors (Dewell and Gabbiani 2018a; Fotowat et al. 2011; McMillan and Gray 2015). Currently, no one has characterized the LGMD's membrane impedance to determine how it shapes this neuron's dendritic integration and visual computations.

Neuronal membranes have mainly been studied with cultured neurons or brain slices, and the natural synaptic input patterns are still unknown for most neurons, so much remains unanswered about how membrane impedance influences synaptic integration and neural computations in vivo. Reduced preparations and modeling have demonstrated that many neurons have pronounced frequency-dependent filtering properties that likely shape the integration of synaptic inputs and spike generation (Rotstein 2017a; Vaidya and Johnston 2013; van Brederode and Berger 2011). The ability to examine the frequency-dependent filtering in vivo in a neuron integrating known synaptic input patterns is a necessary step in understanding dendritic integration. Furthermore, because both active conductances g_H and g_M, mediated respectively by HCN and M channels, are sensitive to numerous modulators (Delmas and Brown 2005; Wahl-Schott and Biel 2009), the ability to conduct experiments in vivo ensures that these channels are in their natural modulatory state. Our results establish that the LGMD membrane impedance is broadband and generates small delays between synaptic currents and V_m changes that remain consistent across membrane potentials. Furthermore, the HCN and M channels, their interactions, and the neuronal morphology all contribute to producing this broadband impedance profile, which increases the LGMD's ability to discriminate behaviorally relevant patterns of synaptic inputs from irrelevant ones.

MATERIALS AND METHODS

Animals. Experiments were performed on adult female grasshoppers 7–12 wk of age (*Schistocerca americana*). Animals were reared in a crowded laboratory colony under 12:12-h light-dark conditions. Animals were selected for health and size without randomization, and investigators were not blinded to experimental conditions. Sample sizes were not predetermined before experiments. The surgical procedures used have been described previously (Dewell and Gabbiani 2018a; Gabbiani and Krapp 2006; Jones and Gabbiani 2012).

Visual stimuli. Visual stimuli were generated with MATLAB (RRID: SCR_001622; see https://scicrunch.org/resources for details) and the Psychophysics Toolbox (PTB-3, RRID: SCR_002881) on a personal computer running Windows XP. A cathode ray tube monitor refreshed at 200 frames/s was used for stimulus display (LG Electronics, Seoul, Korea). Looming stimuli are the two-dimensional projections of an object approaching on a collision course with the animal. They consisted of an expanding dark square simulating a solid object with half-size l approaching at constant speed v (illustrated in Fig. 1*D*). The expansion profile is characterized by the ratio $l/|v|$, as previously described (Gabbiani et al. 2001). Recording methods for visual responses were the same as for current injection experiments (see below).

Electrophysiology. Sharp electrode LGMD intracellular recordings were carried out in current-clamp or voltage-clamp mode with thin-walled borosilicate glass pipettes filled with a 1.0 M KAc, 1.5 M KCl solution yielding electrode resistances of 12–20 MΩ (outer/inner diameter: 1.2/0.9 mm; WPI, Sarasota, FL; see Jones and Gabbiani 2012 and Dewell and Gabbiani 2018a for details). Membrane potential (V_m) and current (I_m) were low-pass filtered with cutoff frequencies of 10 kHz and 5 kHz, respectively. Most recordings were digitized at a sampling rate of 20,073 Hz (for some experiments the V_m was digitized at 40,146 Hz). We used a single-electrode amplifier capable of operating in discontinuous mode at high switching frequencies (20–35 kHz) (SEC-10; NPI, Tamm, Germany). Responses to current injections were recorded in discontinuous current-clamp mode or discontinuous single-electrode voltage-clamp mode. For dual recordings we inserted under visual guidance a second sharp electrode into the excitatory dendritic field of the LGMD with a motorized micromanipulator (Sutter Instruments, Novato, CA; see Fig. 2*A*). V_m was recorded with a second SEC-10 amplifier in bridge mode with electrode resistance and capacitance compensation when not injecting current and in discontinuous current-clamp mode while injecting current. Switching frequencies, signal filtering, and digitization were identical for both recordings. Methods used to inject currents simulating excitatory postsynaptic potentials (EPSPs) at various holding potentials were identical to those described in Dewell and Gabbiani (2018a).

The physical distance along the dendrites and a substitute for the electrotonic distance between recording electrode pairs were measured as follows. First, all cells were stained with Alexa Fluor 594 and imaged with a CCD camera to record electrode positions (Dewell and Gabbiani 2018a). Next, an image of the neuron and electrodes (cf. Fig. 2*A*) was imported into ImageJ (RRID: SCR_003070), the dendritic path between the electrode tips was manually traced, and the corresponding path length was recorded. To assess the relative electrotonic distances between recording locations we measured the amplitude of the back-propagating action potentials (bAPs) from the resting membrane potential to its peak (Fig. 2*E*) at each location and used the difference in these amplitudes. As in a previous study, the differences in bAP amplitude provided a more reliable explanatory variable for distance-dependent effects (Dewell and Gabbiani 2018a).

A neuron's frequency-dependent membrane properties are characterized by its impedance profile. The subthreshold impedance can be decomposed into input impedance (Z_{IN}), which describes local change in V_m at the site of an input current, and transfer impedance (Z_{TR}), which describes change in V_m at remote locations after propagation through the neuron. Both Z_{IN} and Z_{TR} shape synaptic integration within dendrites. Additionally, impedance properties at the site of

spike initiation influence the transformation of V_m into spiking activity, including the frequency filtering and timing of a neuron's output. If a neuron's conductance distribution is uniform, then Z_{TR} and Z_{IN} will have similar properties. When it is not, the impedance profile varies by location and transfer depends on the recording locations and the direction of signal propagation (Hu et al. 2009; Vaidya and Johnston 2013).

To measure the impedance profile, we injected sine waves of increasing frequency called chirp (or zap) currents. To verify that the injected current matched the computer-generated waveform, we recorded I_m simultaneously with V_m. The chirp currents used were identical to those described in Dewell and Gabbiani (2018b). The chirp current is defined as $I(t) = I_p \sin\phi(t)$, where I_p is the peak current, $\phi(t)$ is the phase of the sine wave, and its instantaneous frequency is defined as $f(t) = \frac{1}{2\pi}\frac{d\phi}{dt}$ (in units of Hz). We generally used chirps with a duration of 20 s (sometimes 30 s) that increased in frequency either linearly or exponentially with time. In most experiments, as well as for all simulations, we used exponentially increasing chirp currents. The linear chirp started at 0 Hz and was calculated as $I(t) = I_p \sin(\pi\beta t^2)$, with t being the time from the start of the chirp (in units of s) and β the rate of increase in instantaneous chirp frequency (in Hz/s). The exponential chirp was given by $I(t) = I_p \sin(2\pi f_0 t e^{\beta t})$, where f_0 is the initial chirp frequency and β determines the (accelerating) rate of frequency increase (Barrow and Wu 2009). For all exponential chirps, we used $f_0 = 0.05$ Hz and $\beta = 0.24$ Hz, which produced a chirp current increasing to 35 Hz over 20 s. We saw no differences in the calculated impedance profiles with chirps having different frequency profiles, in accordance with previous comparisons of impedance profiles between chirps of increasing and decreasing frequencies (Erchova et al. 2004; Hu et al. 2002; Ulrich 2002; van Brederode and Berger 2008, 2011) or comparison of linearly increasing chirps and sums of sine wave stimuli (Hutcheon et al. 1996). Before each chirp current a −2-nA hyperpolarizing step current was used for monitoring the input resistance and the membrane time constant (Dewell and Gabbiani 2018b).

Pharmacology. We applied the HCN-channel blocker ZD7288 and the M-channel blocker XE991 either directly in the bath saline or by local puffing as previously described (Dewell and Gabbiani 2018a, 2018b). For local puffing we used a micropipette connected to a pneumatic picopump (PV830; WPI). Drugs were mixed with physiological saline containing Fast Green (0.5%) to visually monitor the affected region. For both delivery methods, drug concentrations within the lobula were ~200 μM for ZD7288 and ~100–200 μM for XE991. In dual-recording experiments, mecamylamine was applied to block EPSPs and was present in both control and drug conditions. Blockade of EPSPs reduced membrane noise as well as noise in the calculated impedance profiles. In paired comparisons mecamylamine caused small increases in impedance amplitude (~5%), but this difference was smaller than the variability between animals or between dendritic locations. For control data we thus pooled recordings with and without mecamylamine.

Experimental design and statistical analyses. Data analysis was carried out with custom MATLAB code (MathWorks, Natick, MA). Linear fits were done by minimization of the sum of squared errors. Unless otherwise specified, values are presented as means ± standard deviation (SD). Dependence of voltage attenuation, phase, and time lag on bAP amplitude differences were initially assessed with a Kruskal-Wallis test (1-way ANOVA on ranks). Results are reported as coefficient of determination (R^2) and the test P value (Fig. 2). Additionally, we computed the Pearson linear correlation coefficient (r) and the associated probability that the slope equals 0 (P). For paired comparisons the Wilcoxon signed-rank test was used, and for unpaired comparisons the Wilcoxon rank sum test was used. Both tests do not assume normality or equality of variance.

The complex impedance Z was calculated as $Z(f) = \text{fft}(V_m)/\text{fft}(I_m)$, where fft is the (frequency dependent) fast Fourier transform, I_m the membrane current, and V_m the membrane potential. Both I_m and V_m were downsampled to 2 kHz before the fft. Z was calculated for each trial and averaged across trials. Z is composed of its real part, the resistance R, and its imaginary part, the reactance X: $Z = R + iX$ (where $i = \sqrt{-1}$). A positive reactance, or inductance, indicates that changes in V_m precede changes in I_m. Conversely, a negative reactance, or capacitance, indicates that changes in I_m precede changes in V_m. The impedance amplitude is calculated as the absolute value of Z: $|Z(f)| = \sqrt{R(f)^2 + X(f)^2}$. The impedance phase is calculated by taking the inverse tangent of the reactance divided by the resistance: $\Phi(f) = \tan^{-1} X(f)/R(f)$. It represents the angle between the x-axis and a line from the origin to a point of the impedance locus plot (cf. Fig. 4, *D* and *E*).

Z_{IN} was calculated from the V_m and I_m recorded at the site of current injection. Z_{TR} was calculated with the I_m from the site of current injection and the V_m from the noninjected site. Z_{IN} reveals the mapping of current to local dendritic membrane potential frequencies, while Z_{TR} also includes the change in membrane potential frequency as the signal propagates from the dendrites toward the SIZ. Voltage attenuation was calculated as the relative reduction in impedance amplitude from the current injection site to the noninjected site: $V_{att}(f) = [|Z_{IN}(f)| - |Z_{TR}(f)|]/|Z_{IN}(f)|$ (Fig. 3*D*). Similarly, the phase lag was calculated as the Z_{IN} minus the Z_{TR} phase (Fig. 4*F*). The Z_{IN} and Z_{TR} phases were each converted to the time domain by $t_{phase}(f) = \Phi(f)/(2\pi f)$, where f is the instantaneous chirp frequency (in Hz) calculated as $f(t) = \frac{1}{2\pi}\frac{d}{dt}\sin^{-1}\left[\frac{I(t)}{I_p}\right]$; for details see Dewell and Gabbiani (2018b). The mean Z_{IN} and Z_{TR} delays were then calculated by averaging across frequencies (0–35 Hz) the absolute value of the delay between the input current and membrane potential at the two recording locations (Fig. 4*G*).

Resonance in an electrical circuit is characterized by its bandwidth and strength (the Q factor; Horowitz and Hill 2015). Resonant strength was calculated from the Z_{IN} amplitude as the ratio of the maximum impedance to the steady-state (0.1 Hz) impedance (Koch 1984). This measure ignores impedance at other frequencies. So, we also characterized the variability of the impedance amplitude by its SD across frequencies normalized to the mean impedance amplitude, which we call the frequency variation (f_{var}; Fig. 3*E* and Fig. 5*G*). It was calculated across frequencies ranging from 0 to 35 Hz. Unlike resonance strength, f_{var} incorporates both the strength and breadth of the bandpass. An ideal resistor would have a f_{var} of zero, whereas a membrane exhibiting sharp band-pass attributes would produce high frequency variation. For a sense of scale, a single-compartment model with the same time constant as the LGMD and no active membrane properties would be low pass and have $f_{var} = 18.4$. In contrast, active models with a large, slow inductance were resonant and had f_{var} values up to 378 (see below; Supplemental Fig. S2*B*, https://doi.org/10.5281/zenodo.2635829). This statistic depends on the frequency range examined, limiting the ability to compare values between studies examining different frequency ranges.

For calculating the power density of the membrane potential, we used the MATLAB multitaper power spectral density estimate (function "pmtm"), with a time-half bandwidth product of 4 measured over 15 octaves at frequencies of 2^{-4} to 2^{11} Hz with 8 voices (scales) per octave. The mean was subtracted from all data before calculation of the power density estimate, and the resulting estimates were averaged across trials. For estimating the time-varying power density we used MATLAB's continuous wavelet transform (function "cwt"). The frequency range was set from 0.1 to 2,000 Hz, and the signal was not extended. As for the spectral density estimate, wavelet transforms were calculated for individual trials and the resulting wavelet trans-

form coefficients were averaged across trials. In the calculation of both measures, the raw data were used.

Electrical circuit model. The LGMD membrane impedance was compared to the impedance of an equivalent cable based either on RC or RLC circuits. RC circuits describe passive membranes, whereas RLC circuits can approximate the frequency-dependent properties of active neuronal membranes. Active conductances are both frequency and voltage dependent, whereas inductances are only frequency dependent. The RLC circuit was modeled as illustrated in Supplemental Fig. S2*A*. The membrane impedance density was calculated as

$$Z_m = \frac{R_m}{1 - l_{rat} + l_{rat}/\left(1 + i\tau_L\omega\right) + i\tau_m\omega}$$

where Z_m is the Z_{IN} density (in units of $M\Omega cm^2$), R_m is the membrane resistivity ($M\Omega cm^2$), τ_m (s) is the membrane time constant ($\tau_m = R_m C_m$), C_m is the membrane capacitance ($\mu F/cm^2$), τ_L is the inductance time constant (s), ω is frequency (rad/s), l_{rat} is the fraction of the membrane conductance that is in series with the inductor (range [0–1]), and $i = \sqrt{-1}$. If l_{rat} is 0, then no current passes through the inductor and the circuit is equivalent to an RC circuit with impedance

$$Z_m = R_m/\left(1 + i\tau_m\omega\right)$$

In both cases, Z_{IN} was calculated by dividing Z_m by the unit surface area of the cable (cm^2). We used the average dendritic circumference of our full LGMD model (20.85 μm) for the cable circumference.

Z_{TR} measures were based upon a cable of fixed diameter and infinite length. The voltage transfer along the cable was calculated as $V_{TR} = e^{-l/\lambda}$, where l (cm) is the distance between the two locations and λ is the cable's length constant (cm), $\lambda = \sqrt{Z_m/(R_a d b_f)}$. R_a is the axial resistivity (Ωcm), d is the diameter (cm), and $b_f = 3$ is the branch factor, a scalar added to account for additional attenuation due to the dendritic branching. Z_{TR} at distance l from the site of current injection is the product of Z_{IN} and V_{TR}.

Simulations of morphological neuron models. These simulations build upon earlier ones that examined the role of morphology on signal propagation and impedance (Holmes et al. 1992; Jaffe and Carnevale 1999; Mainen and Sejnowski 1996; Vetter et al. 2001). The principal difference is the characterization of morphological influence on the impedance delay and calculation of the net influence of morphology on input currents distributed throughout the dendritic arbors.

The cell morphologies used were based on either neuronal reconstructions or straight cables and a simplified Rall model (Rall 1964). The cable models differed in diameter but were all 0.5 cm in length subdivided into 100 sections 5 μm long. Three cables had uniform diameters of 2, 10, or 20 μm, one had diameters tapering linearly from 50 μm at one end to 0.5 μm at the other, and one cable model had 100 random section diameters selected from a uniform distribution between 0.5 and 39.5 μm. The Rall models (illustrated in Fig. 7*A* and Supplemental Fig. S3*A*, https://doi.org/10.5281/zenodo.2635831) had 64 sections, each 20 μm long. The soma had a 20-μm diameter, and the dendritic arbor had 5 branch levels. The base branch had a 12-μm diameter, with each level decreasing in diameter according to the 2/3 power law (Rall 1964). The "pinched" Rall model (Fig. 7*A*, *bottom*) differed from the conventional Rall model (Supplemental Fig. S3*A*) because we decreased the diameter of each dendritic branch fivefold over the segment immediately distal to each branch point. Each branch of the model contained 5 segments.

For the realistic neuronal morphologies, we selected neurons spanning a wide range of branching patterns and sizes from the ModelDB repository (RRID: SCR_007271). They included a cerebellar Purkinje neuron (Miyasho et al. 2001; Ostojic et al. 2015), a CA1 pyramidal neuron (Migliore et al. 2004), an oriens-lacunosum/moleculare (OLM) hippocampal interneuron (Sekulić et al. 2015), and a human layer 2/3 temporal cortex pyramidal neuron (Eyal et al. 2016). All models were passive with identical membrane properties close to those used in the LGMD model (Fig. 6*C*). The LGMD model (Fig. 6*C*) and a reduced version in which an electrotonically equivalent cable replaced each of its three dendritic trees were used as well (Fig. 7*A*, *bottom*; Dewell and Gabbiani 2018a). All simulations were carried out with the NEURON software simulation package. For a passive model, measuring impedance with chirp currents, as was done experimentally, or with NEURON's built-in impedance tools yielded the same result, so we used the built-in impedance measurement to speed up the simulations.

In Fig. 6*G*, the percentage of cell surface area with improved Z_{TR} amplitude was calculated from the data depicted in Fig. 6*F*, *right*. Specifically, we calculated the Z_{TR} amplitude between all neuron segments (axial resistivity of 350 Ωcm) and compared it to the impedance amplitude of an isopotential model using the same cell morphology with axial resistivity set to 0. Although setting the axial resistivity to 0 is not realistic, this method provides a simple way of preserving the total membrane area, conductance, and capacitance of the model. The impedance amplitude of an isopotential cell is $R/\left(1 + \tau_m^2\omega^2\right)^{0.5}$, where R is the membrane resistance ($M\Omega$), ω is the frequency (s^{-1}), and τ_m is the membrane time constant (s). As C_m and R_m were the same for all morphologies ($C_m = 0.8$ $\mu F/cm^2$, $R_m = 10$ $M\Omega cm^2$), their membrane time constants were the same ($\tau_m = R_m C_m$) whereas the membrane resistance changed with their total membrane area A ($R = R_m/A$). For each segment, we summed the surface area of all segments to which a broadband signal transferred with greater gain than the isopotential value (Fig. 6*F*, *right*) and divided by the neuron's total surface area. Frequencies of 0–1,000 Hz were used and averaged with equal weight.

Similarly, to obtain Fig. 6*I* we computed the Z_{TR} phase between all segment pairs and compared it to the impedance phase of an isopotential equivalent. The impedance phase of an isopotential cell is $\tan^{-1}(-\tau_m\omega)$. For the phase measurements, a weighted average was used, with the transfer amplitude between the segment pair determining the weight for each frequency. As signals of some frequencies transfer better than others, the transfer phase of these signals influences the membrane synchrony more. The percentage of area with increased impedance phase was then calculated by summing the surface area of segments with more synchronous transfer phase than an isopotential equivalent cell and dividing by the total membrane surface area of the neuron. These calculations measure the average signal transfer of a passive cell with realistic morphology receiving broadband inputs with a uniform density. Although these simplifying assumptions would not necessarily hold in vivo, where the location and frequency of inputs are constantly changing, they allow one to estimate Z_{TR} without relying on the less realistic assumptions that all inputs impinge on a single location or that all signals integrate at a single location, like the neuron's SIZ.

Input synchrony simulations. The LGMD detects approaching objects by discriminating differences in excitatory input synchrony of tens of milliseconds (Jones and Gabbiani 2010). To address whether g_H and g_M help discriminate input timing, we adapted simulations showing that g_H increases the ability of a CA1 pyramidal neuron to discriminate the timing of its excitatory synaptic inputs (Migliore et al. 2004; simulation code available: https://senselab.med.yale.edu/ModelDB/showmodel.cshtml?model=32992). In such simulations, a barrage of excitatory synaptic inputs impinges on a subset of dendritic branches with varying degrees of temporal synchrony. The input synchrony is altered with the addition of a random temporal jitter applied to each input. We expanded on these results by testing whether the voltage dependence or inductive properties of g_H and g_M underlie this effect (Fig. 8). To control inductance independently of voltage dependence, we created a membrane channel (inductive leak) that has a conductance inversely dependent on the rate of change of the membrane potential, thus implementing a high-pass filter. Although these simulations do not address directly how the LGMD detects synchrony in the context of looming, their simplicity makes the interpretation of the results straightforward and generalizable to other biophysical models.

Model availability. The files required to reproduce Figs. 6–8 and Supplemental Figs. S3 and S4 are available on ModelDB (https://ModelDB.yale.edu/256024).

RESULTS

Spectral power density of the LGMD's membrane potential is concentrated at low frequencies. The LGMD possesses three dendritic fields, with the largest one, field A, integrating excitatory inputs originating from every facet of the compound eye (Fig. 1*A*). It responds discriminately to approaching objects that activate thousands of facets based on the object's trajectory and spatial coherence (Dewell and Gabbiani 2018a; Gray et al. 2001). To determine the signal frequencies most relevant to the LGMD, we measured the spectral power density of its V_m. We first measured the power spectrum of the V_m for spontaneous activity. The LGMD receives a high number of spontaneous synaptic inputs (Fig. 1*B*; Jones and Gabbiani 2012), and its membrane time constant is short in vivo (~7 ms; Dewell and Gabbiani, 2018a, 2018b; Gabbiani and Krapp 2006; Peron et al. 2007). This raises the possibility that high-frequency components might dominate the LGMD's V_m power spectrum. However, we found that 87% of the power was contained below 35 Hz, with 50% below 7.5 Hz (Fig. 1*C*).

Next, we computed the spectral power density in response to the simulated approach of objects on a collision course, looming stimuli (Fig. 1*D*). During the course of such a stimulus the number of activated ommatidia increases from ~10 to >2,500, producing an increase in activated synapses from ~100 to >20,000 (Rind et al. 2016). As this increased synaptic input occurs in ever tighter time windows leading to an increase and peak in V_m and firing rate (Fig. 1*E*), it might lead to a shift in power toward higher frequencies. However, low-frequency power increased during looming stimuli, with >50% of it below 1.5 Hz (Fig. 1*C*). As most of the membrane depolarization and spiking activity generated by looming occurs over the last second before collision, we also used wavelet analysis to resolve the frequency content of the V_m in the time domain (see MATERIALS AND METHODS). When compared with an equivalent period of spontaneous activity analyzed similarly (Supplemental Fig. S1; https://doi.org/10.5281/zenodo.2635818), there was an increase in power spectral density at higher frequencies (Fig. 1*F*). However, most power remained centered around 1–2 Hz (Fig. 1*F*). The concentration of the LGMD membrane potential power at low frequencies despite high-frequency synaptic input could be due to the activation characteristics of

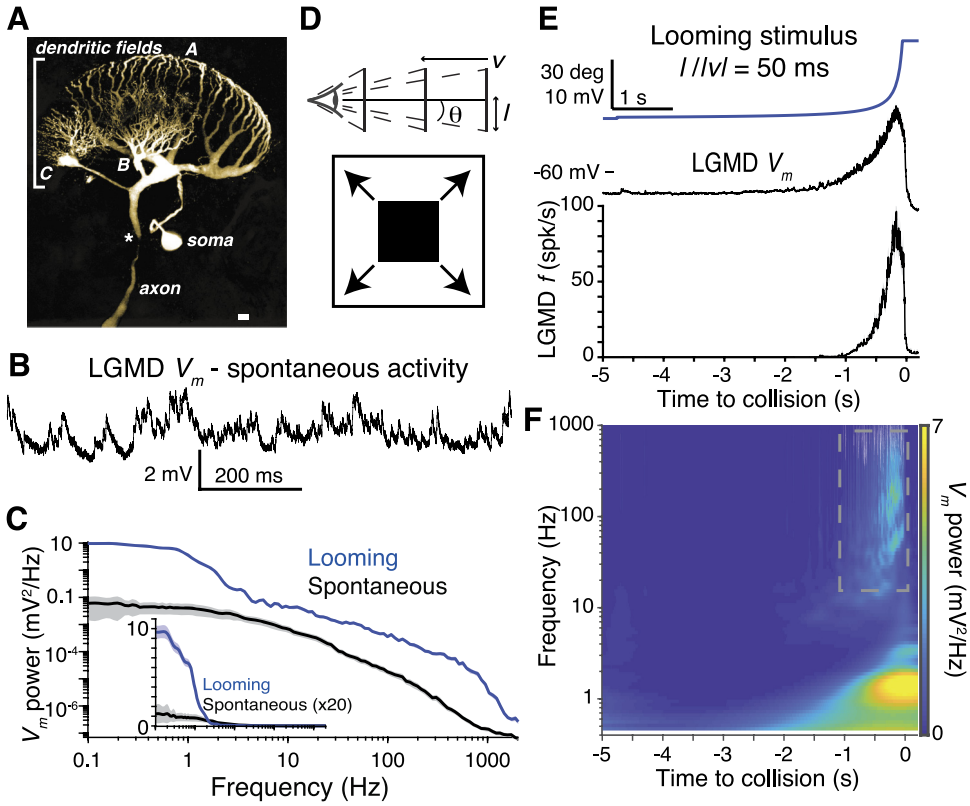

Fig. 1. Spontaneous and looming stimulus-evoked spectral power density of the lobula giant movement detector's (LGMD) membrane potential. *A*: micrograph of the LGMD, illustrating its dendritic fields (labeled A, B, and C), the spike initiation zone (marked with *) at the start of the axon, and the soma, which lies outside of the neuron's electrical signal path (adapted from Gabbiani et al. 2002 with permission). Scale bar, 25 μm. *B*: example recording of dendritic membrane potential within the LGMD while the eye was exposed to uniform illumination (V_m low-pass filtered at 10 kHz and digitized at 40 kHz). *C*: V_m power was concentrated at frequencies below 5 Hz (black; axes on logarithmic scale). During looming stimuli, the signal power increased 125-fold but remained concentrated at low frequencies (blue). *Inset*: the data with a linear *y*-axis scale; solid lines and shaded regions are means ± SE (16 animals). *D*: a looming stimulus consists of a black square expanding symmetrically on the animal's retina (*bottom*). It simulates an object of half-size *l* approaching on a collision course at constant velocity v (< 0), subtending an angular size $2\theta(t)$ at the retina (*top*). *E*: looming stimuli produce an angular size that increases nonlinearly over time (*top*, blue line). Most of the response to looming stimuli occurs shortly before the projected time of collision, as can be seen in the average membrane potential (V_m, *middle*) and firing rate (*f*; *bottom*, displayed as mean ± SE for 59 looming stimuli in 16 animals). *F*: wavelet analysis of the V_m power density reveals that during spiking there is increased high-frequency power (dashed rectangle), but the peak power remains at frequencies <10 Hz. Plot displays the average power density map of the same 59 looming responses shown in *C* and *E*.

these inputs or to low-pass filtering by the LGMD's membrane. We tested the latter possibility by measuring the frequency-resolved input and Z_{TR} of the LGMD's membrane.

Single and dual dendritic LGMD recordings in vivo in response to chirp currents. The LGMD's Z_{IN} and Z_{TR} were measured in vivo by injecting chirp currents during single or paired recordings in the excitatory dendritic field (see MATERIALS AND METHODS; Fig. 2*A*). Superposing chirp currents on different holding currents allowed us to measure impedance at multiple steady-state membrane potentials (V_{ss}; Fig. 2*B*), and thus at different steady-state activation levels of subthreshold conductances present in the LGMD membrane. In general, chirp responses looked consistent across V_{ss} values, tapering slightly with increasing frequency. Examination of different periods of the chirp show that at low frequencies the oscillations in I_m and V_m were synchronous, whereas at higher frequencies the V_m lagged behind the current and the change in potential was smaller (Fig. 2*C*). We conducted similar experiments in voltage clamp and found similar changes to occur (Fig. 2*D*).

Quantification of Z_{TR} characteristics was made as a function of the distance between 11 pairs of dendritic recordings (from 8 animals). The interelectrode distance was measured both as the dendritic path length between the electrodes in experimental micrographs (path distance; Fig. 2*A*), and as the difference in bAP amplitudes (an indirect measure of the electrotonic distance; Fig. 2*E*). bAP amplitude was ~40 mV at the base of the excitatory dendritic field and decayed to <10 mV in distal dendritic branches. The recording locations in the present study were in larger branches with bAP amplitudes between 20 and 40 mV. The path distances between these electrode pairs ranged from 63 to 150 μm. The difference in bAP amplitudes was well correlated with changes in membrane potential transfer properties (Fig. 2*F*). In contrast, there was less correlation between path distance and voltage attenuation [$r(9) = 0.17$, $P = 0.63$, Pearson linear correlation], likely because of differences in dendrite diameter or number of branch points between the recording pairs. With increased electrotonic distance between recording pairs, there was an increased voltage attenuation and delay. The electrotonically closest recordings had ≤10% voltage attenuation, whereas for distant pairs this value increased to almost 50% (Fig. 2*F*, *top*). The average phase and time lags (0–35 Hz) between locations were ~3° and 0.5 ms between the most synchronous pairs and ~10° and 2 ms between the most asynchronous pairs (Fig. 2*F*). For subsequent analyses of Z_{TR}, data from all recording pairs were pooled.

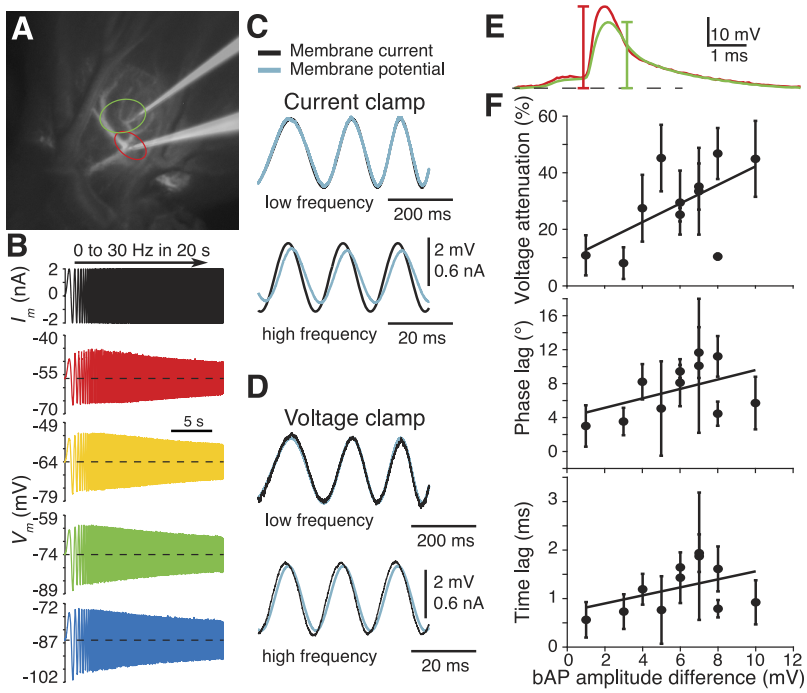

Fig. 2. Characterization of lobula giant movement detector's (LGMD) membrane impedance profile with in vivo dendritic recordings. *A*: either single or dual recordings were made from dendritic field A and the primary neurite connecting field A to the spike initiation zone. Image taken with a CCD camera during a dual recording after staining the LGMD with Alexa Fluor 594. The internal solution of both electrodes contained Alexa Fluor 594 for visualization. Red and green ellipses encompass the region sampled by the proximal and distal electrodes, respectively, across 11 recording pairs (8 animals). *B*: to measure membrane impedance, chirp currents (sine waveforms of increasing frequency) were injected at different steady-state membrane potentials (V_{ss}). At *top* is an example of a linearly increasing chirp current (I_m) followed by 4 recordings of the membrane potential (V_m) in response to this chirp current superposed on different holding currents (I_{hold}). The values of I_{hold} and V_{ss} (dashed lines) were 2, 0, −2, −4 nA and −56, −64, −74, −86 mV, respectively (from *top* to *bottom*). *C*: example traces of low- and high-frequency sections of the measured membrane current and potential. At low frequencies the current and potential are synchronous (~0° impedance phase), but at high frequencies the potential trails the current (negative impedance phase). Note that at high frequencies the membrane potential is reduced relative to the current, indicating a reduction in impedance amplitude. *D*: impedance properties were similar when measured in voltage clamp. *E*: example traces of backpropagating action potentials (bAPs) from the 2 recording electrodes and bars indicating that the bAP amplitudes were measured from the resting membrane potential to their peaks. The trace colors correspond to the electrode positions in *A*. Mean bAP amplitudes were 32 and 26 mV for the proximal and distal electrode, respectively. *F*: as the relative electrotonic distance increased between recording electrodes (estimated by the difference in amplitudes of the bAP), there was an increase in attenuation (*top*; $R^2 = 0.40$, $P = 3.2 \times 10^{-6}$), in the phase lag (*middle*; $R^2 = 0.17$, $P = 1.9 \times 10^{-4}$), and in the time lag (*bottom*; $R^2 = 0.15$, $P = 2.7 \times 10^{-4}$). Each point and error bar report the mean value and SD (across different V_{ss} values) for a recording pair (11 recording pairs from 8 animals).

Consistency of impedance amplitude across holding potentials and chirp frequencies. We measured the impedance amplitude at different V_{ss} values and examined how its profile changed with holding potential. The LGMD dendrites have a resting membrane potential near −65 mV, can be hyperpolarized by inhibitory inputs to below −70 mV, and are depolarized by excitatory inputs to over −50 mV during looming stimuli (Fig. 1*E*). We thus used V_{ss} values spanning that range and confined below the spike threshold potential.

The observed impedance amplitude profiles are shown in Fig. 3*A*. Within animals they were consistent across trials and holding potentials, with 91.1% and 95.8% median similarity to the individual mean for Z_{IN} and Z_{TR}, respectively (Fig. 3*B*). About half of this trial variability was explained by the holding potential (mean R^2 of relationship between V_{ss} and residual 0.53 ± 0.38 for Z_{IN} and 0.45 ± 0.36 for Z_{TR}; 304 V_{ss} values from 53 recordings for input and 81 V_{ss} values from 11 recordings for Z_{TR}). On average Z_{IN} decreased by 0.032 MΩ/mV (Fig. 3*C*), and 27 of 53 recording locations had a significant reduction in Z_{IN} with increased depolarization ($r < -0.6$, $P < 0.01$; Pearson linear correlation). Z_{TR} changed even less with holding potential: on average a 0.006 MΩ/mV decrease (Fig. 3*C*).

The constancy of impedance amplitude implies a constant total membrane conductance across holding potentials. Although other channels might contribute, HCN and M channels account for the majority of the LGMD's resting membrane conductance, suggesting that their total conductance remains roughly constant. This in turn should increase the consistency of EPSP amplitudes across holding potentials. This was confirmed by injecting currents simulating EPSP waveforms at the same V_{ss} values used to measure impedance, resulting in peak depolarizations that were independent of V_{ss} [$r(89) = -0.05$, $P = 0.63$; 91 V_{ss} values from 16 recordings in 9 animals].

In addition to the consistency across holding potentials, the Z_{IN} and Z_{TR} amplitudes changed little with frequency (Fig. 3*A*). This differs from other HCN and M channel-expressing neurons that exhibit a pronounced resonant frequency (Gastrein et al. 2011; Gutfreund et al. 1995; Hu et al. 2002; Hutcheon et al. 1996). Similarly, the voltage attenuation between paired recording locations showed no preferred frequency (Fig. 3*D*). The variability of the voltage attenuation was higher though, because of the differences in electrotonic distance (Fig. 2*F*). The frequency variation of the LGMD's Z_{IN} amplitude was 10–15% and decreased slightly with membrane depolarization (Fig. 3*E*; f_{var}, see MATERIALS AND METHODS). Z_{TR} amplitude had a frequency variation of ~20% and also decreased with depolarization (Fig. 3*E*). To test what electrical components could produce the impedance amplitude properties of the LGMD, we created an array of RC and RLC circuit models (Supplemental Fig. S2*A*), as in earlier studies (Koch 1984; Mauro 1961; Rall 1964). The observed impedance frequency variations were below those of either low-pass or band-pass circuits with a comparable time constant and could not be replicated by any model with slower time constants (Supplemental Fig. S2, *B* and *C*). The circuit models suggest that the low frequency variation of the LGMD's impedance profile depends on a fast inductance (<20 ms) in addition to its fast membrane time constant (6.9 ms; Dewell and Gabbiani 2018a, 2018b; Gabbiani and Krapp 2006; Peron et al. 2007). Of the LGMD's known conductances, g_M is the most likely candidate to provide such a fast inductance.

The V_m power spectral density at 0 Hz was 1,000-fold higher than at 35 Hz during looming stimuli and 25-fold higher during

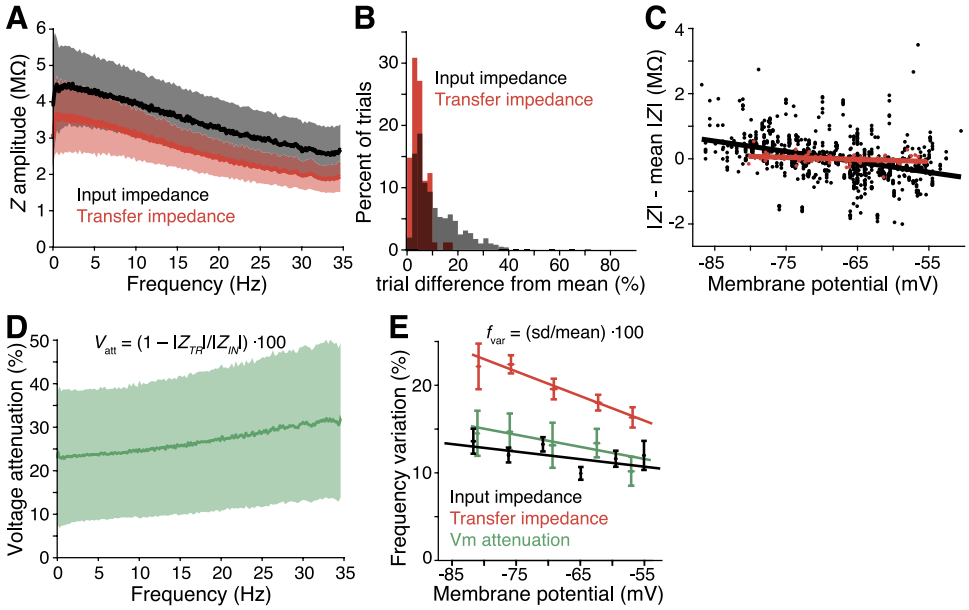

Fig. 3. Lobula giant movement detector (LGMD) membrane impedance amplitude and voltage attenuation decrease slightly with frequency and membrane potential (V_m). *A*: input (Z_{IN}) and transfer (Z_{TR}) impedance amplitude profiles displayed as means ± SD (lines and shaded regions): 53 recordings from 47 animals for Z_{IN} and 13 recordings from 10 animals for Z_{TR}. *B*: histogram of similarity of individual trials to the recording mean impedance profile measured at different steady-state membrane potentials (V_{ss}, see Fig. 2*B*): 81 V_{ss} values for Z_{TR} and 304 V_{ss} values for Z_{IN}. *C*: the impedance amplitude (plotted relative to the recording mean) decreased with depolarization. Input amplitude decreased by 0.032 MΩ/mV ($r = -0.40$, $P = 7.6\times 10^{-9}$), and transfer amplitude decreased by 0.006 MΩ/mV ($r = -0.32$, $P = 0.004$; Pearson linear correlations). *D*: voltage attenuation (V_{att}) had higher variation between recordings than impedance amplitude (mean coefficient of variation of 0.61 for attenuation and 0.22 for transfer amplitude), with ~20–35% reduction in voltage between dendritic locations. Same recordings as for Z_{TR}. *E*: the frequency variation (f_{var}) of the input and transfer impedance amplitude as well as that of voltage attenuation decreased slightly with membrane depolarization. The f_{var} shows consistency across frequencies, with a value of 0 indicating an ideal resistor.

spontaneous inputs (Fig. 1, *C* and *F*). For the same frequencies, both the Z_{IN} and Z_{TR} amplitudes were less than twofold higher (Fig. 3*A*). If the synaptic inputs during looming were broadband and the low-pass spectral density were due to membrane filtering, this would imply a low-pass membrane with a frequency variation >250%. This suggests that the low-frequency power is due to the activation characteristics of the synaptic input currents during a looming stimulus.

Impedance phase reveals high current-voltage synchrony across membrane potentials. Membrane capacitance produces a phase lag between input currents and changes in membrane potential that increases with frequency and distance of propagation. Conductances like g_H and g_M counteract this lag (Hu et al. 2009; Narayanan and Johnston 2008; Ulrich 2002; Vaidya and Johnston 2013). To characterize the timing of the LGMD's membrane potential changes with respect to current inputs, we measured the dendritic impedance phase. In a passive, isopotential neuron, membrane capacitance forces the Z_{IN} phase to saturate at −90° as input current frequency increases (Mauro 1961; Narayanan and Johnston 2008). Conversely, a positive impedance phase indicates that the change in voltage precedes the change in current, a feature requiring a physiological process that resembles an electrical inductance. Although the LGMD's impedance phase decreased with frequency, it saturated well above −90° and in some recordings even increased at frequencies >20 Hz. This was the case for both the Z_{IN} and Z_{TR} phase (Fig. 4*A*). For all holding potentials, the phase was positive at low frequencies (<1 Hz; Fig. 4*B*) and the subthreshold membrane potential was most synchronous (zero phase) with input current at ~1 Hz, in contrast to spiking, which is most synchronous with input currents of ~6 Hz (Dewell and Gabbiani 2018b).

Like impedance amplitude, impedance phase varied less with V_{ss} values than in other neurons (Gutfreund et al. 1995; Narayanan and Johnston 2008). On average the phase increased with depolarization by 0.13°/mV and 0.12°/mV for Z_{IN} and Z_{TR}, respectively (Fig. 4*C*). The input phase of 21 of 53 recording locations significantly increased with membrane potential ($r > 0.6$, $P < 0.01$, Pearson linear correlation), but 0 of 13 recordings showed a significant increase in transfer phase with depolarization ($P > 0.01$ for all recordings).

Plotting as in Fig. 4*D* the real and imaginary components of Z_{IN}, called respectively resistance and reactance, illustrates the low-frequency inductive and the high-frequency capacitive properties of the impedance (corresponding to positive and negative reactance, respectively). The input reactance was consistent across V_{ss} values, whereas the input resistance increased at hyperpolarized potentials, resulting in a rightward shift of the curves as V_{ss} decreased (Fig. 4*D*). The locus plot of Z_{TR} reveals even less change across membrane potentials, with only a small increase in transfer resistance at hyperpolarized potentials (Fig. 4*E*). The relative phase of Z_{IN} and Z_{TR} is the membrane potential phase lag, with larger values indicating increased transfer delay caused by capacitive filtering during

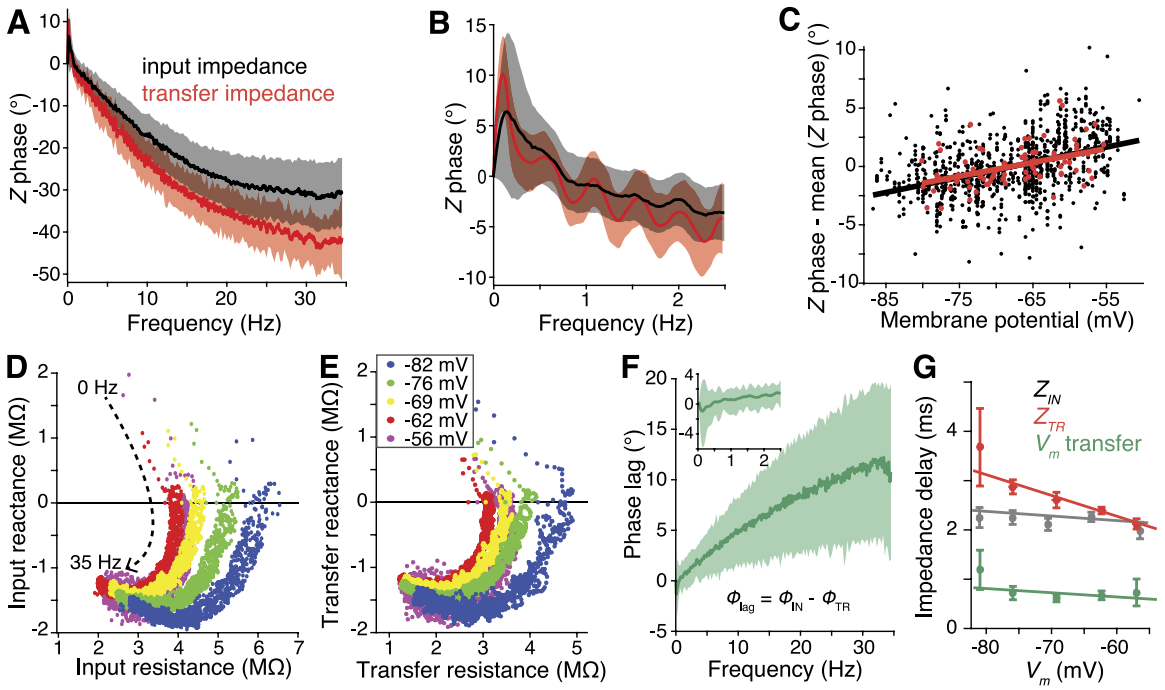

Fig. 4. Lobula giant movement detector (LGMD) membrane synchrony and consistency across membrane potentials. *A*: input (Z_{IN}) and transfer (Z_{TR}) impedance phase profiles (mean ± SD) level off around −30° and −45°. Z_{IN}: 53 recordings from 47 animals. Z_{TR}: 13 recording pairs from 10 animals. *B*: the same data in *A* at an expanded scale show that the phases for both Z_{IN} and Z_{TR} were inductive (exhibited positive phase) at frequencies < 1 Hz. *C*: the phase increased slightly with depolarization. For Z_{IN} the increase was 0.13°/mV ($r = 0.42$, $P < 1 \times 10^{-6}$) with 304 steady-state membrane potential (V_{ss}) values from 53 recordings. Z_{TR} increased 0.12°/mV ($r = 0.46$, $P = 1.6 \times 10^{-5}$) with 81 V_{ss} values from 13 recordings. *D* and *E*: impedance locus plots show the real (resistance) and imaginary (reactance) components of the impedance, pooled across frequencies (dashed arrow). The membrane inductance at low frequencies is evidenced by the points with positive reactance. At hyperpolarized potentials, resistance increased but otherwise the LGMD maintained a consistent profile across membrane potentials. *F*: phase (ϕ) lag of membrane potential (V_m) at the "recording-only" location relative to that at the "recording and current injection" location. At frequencies <1 Hz there was a phase advance, with the more distant location preceding the input location (*inset*). The phase lag increased steadily with frequency. *G*: Z_{IN} and Z_{TR} delay are the lag between the input current and local V_m at the 2 recording locations. V_m transfer delay is the mean lag between V_m at the 2 recording locations. Z_{TR} delay decreased with membrane depolarization ($P = 0.0002$), unlike Z_{IN} ($P = 0.22$) or V_m transfer ($P = 0.33$).

propagation (Fig. 4*F*). The lag between input and transfer phase was negative (inductive) at frequencies ≤ 1 Hz (Fig. 4*F*, *inset*). The low-frequency inductive characteristics of Z_{IN} and Z_{TR} are consistent with the presence of the slowly rectifying HCN conductance in the LGMD's dendrites (Dewell and Gabbiani 2018a).

Signal frequencies with zero reactance have no delay between membrane current and potential. On average, the LGMD's membrane potential and current were offset by ~2 ms at the input location independent of V_{ss} (Fig. 4*G*). The mean delay of the Z_{TR} was ~3 ms at V_{ss} near −80 mV and decreased with depolarization (Fig. 4*G*). We similarly measured the delay in V_m recorded at two positions, which was ≤1 ms (Fig. 4*G*). The Z_{TR} delay decreased by 0.04 ms/mV ($r = -0.40$, $P = 0.0002$; Pearson linear correlation), whereas the Z_{IN} delay and membrane potential lag both decreased <0.01 ms/mV (input: $P = 0.22$, lag: $P = 0.33$). We tested whether an isopotential RLC model with the same conductance and membrane time constant as the LGMD could reproduce such short impedance delays. None could (Supplemental Fig. S2, *D* and *E*), suggesting the presence of additional synchronizing sources.

HCN and M channels reduce impedance amplitude and frequency variation. To assess the influence of HCN and M channels, we measured the LGMD's Z_{IN} before and after addition of two channel specific blockers: ZD7288 and XE991, respectively. Blocking g_H reduces the resting membrane potential and increases input resistance (Dewell and Gabbiani 2018a), so after HCN blockade we applied chirps with lower peak current and higher holding current to generate equivalent V_{ss} values and changes in membrane potential (Fig. 5*A*). After g_H blockade a decrease in the membrane potential was seen with increasing chirp frequencies. The impedance amplitude doubled at low frequency and decreased more steeply with input frequency (Fig. 5*B*). A reduction in inductance was also clear from the decreased impedance phase (Fig. 5*C*).

Blockade of g_M increases the resting membrane potential and input resistance (Dewell and Gabbiani 2018b), so we used decreased holding currents and chirp amplitudes after blockade. After g_M blockade, a resonance emerged (Fig. 5, *D* and *E*). The impedance phase increased at frequencies ≤ 2 Hz and decreased at higher frequencies (Fig. 5*F*). These effects suggest that, in addition to producing inductance evident above 2 Hz, g_M also counteracts an additional inductance that increases impedance amplitude at frequencies around 4 Hz and phase at frequencies ≤ 2 Hz.

Both g_M and g_H reduced frequency variation, causing a larger reduction at depolarized and hyperpolarized potentials, respectively, consistent with their activation kinetics (Fig. 5*G*). We also calculated the resonance strength (MATERIALS AND METHODS) and found it to be small in control conditions (median 1.11), although it increased with depolarization by 0.008 per millivolt of V_{ss} ($r = 0.48$, $P = 6.3 \times 10^{-12}$; 304 V_{ss} values; Fig. 5*H*). The depolarized resonance strength (at $V_{ss} \geq -65$ mV) increased after g_M block from 1.23 ± 0.16 in control to 1.91 ± 0.89 (53 recordings from 47 animals for control, 6 recordings from 6 animals for g_M block; $P = 0.01$, Wilcoxon rank sum test; Fig. 5*H*). For the resonant trials (strength > 1.1) the resonant frequency did not change significantly after g_M block (2.6 ± 3.4 Hz for control and 3.5 ± 1.2 Hz after block, $P = 0.13$). This resonance likely helps generate the increased spiking observed in response to ~3.5-Hz current inputs following g_M blockade (Dewell and Gabbiani 2018b). Although we did not measure the effects of g_H and g_M blockade on Z_{TR}, input and transfer resonance were similar in control conditions. Transfer resonance strengths were only 0.004 ± 0.05 higher than input ones, while transfer resonance frequency was 0.17 ± 1.1 Hz higher ($P = 0.69$ and 0.63, respectively, signed-rank tests; 81 V_{ss} values from 13 recordings). So, the changes in transfer resonance after channel block would likely parallel those of input resonance.

In addition to reducing the impedance amplitude and making it more consistent across frequencies, both g_H and g_M decreased the delay between input current and the resulting change in membrane potential. After blockade of either channel the Z_{IN} delay increased, with g_M blockade having the largest effect (Fig. 5*I*). After g_M blockade, the minimum phase was more capacitive at high frequencies and the maximum phase more inductive at low frequencies (Fig. 5*F*). After g_H blockade, the Z_{IN} phase decayed to a minimum at a lower frequency (Fig. 5*C*). Even after block of the channels, the delay between I_m and V_m was smaller than in an RLC circuit model (compare Fig. 5*I* and Supplemental Fig. S2*E*). This suggests that there must be an additional mechanism that further reduces the delay.

Neuronal morphology increases membrane gain and high-frequency synchrony. To test the influence of morphology on membrane impedance we compared simulations between passive models that either had realistic compartmentalization or were isopotential (otherwise identical models with zero axial resistance; MATERIALS AND METHODS). Plotting the Z_{IN} delay revealed the variability between sections of the full LGMD model (Fig. 6*A*). Additionally, the increased compartmentalization reduced local input delays from that of an isopotential model (Fig. 6*A*). The model segments had a mean input delay of 2.1 ± 1.1 ms, matching experimental data (cf. Fig. 4*G*). This suggests that morphology plays a bigger role in the LGMD membrane potential delay relative to input current than its active properties. The Z_{IN} amplitude for each section predictably decayed less with frequency because of the axial resistivity, although the amount of change varied by cell region (Fig. 6*B*). The input frequency variation of the model sections was 8.6 ± 4.7% for the physiologically dominant frequency range (<35 Hz; see Fig. 1), demonstrating that LGMD compartmentalization alters the Z_{IN} amplitude profile as much as its active conductances. These changes are readily explainable by the model's axial resistivity, which allows for local changes to be less influenced by the membrane capacitance of the rest of the neuron and are not unique to the LGMD.

To compare these effects to those in other neurons, we conducted similar simulations using four neuronal morphologies covering a range of sizes and branching patterns (Fig. 6*C*). They were taken from cerebellar Purkinje, neocortical layer 2/3 pyramidal, CA1 pyramidal, and CA1 OLM neurons. Additionally, we conducted simulations on a Rall branching neuron model, straight cables, and an LGMD model whose dendritic fields were collapsed into an electrotonically equivalent cylinder (Dewell and Gabbiani 2018a). The membrane conductance and capacitance were uniform for all models, producing a membrane time constant of 8 ms (simulations with slower τ_m yielded qualitatively similar results). For all morphologies Z_{IN} delay decreased and amplitude increased relative to their isopotential equivalents. The overall size of each neuron had no

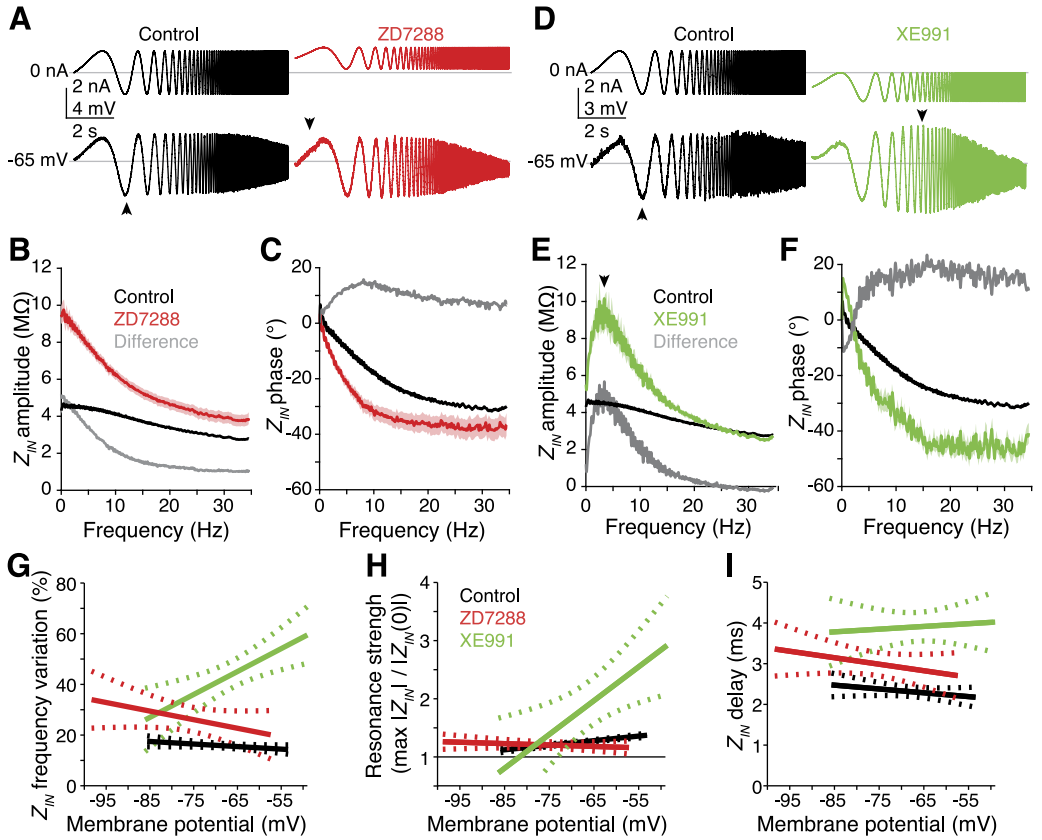

Fig. 5. Blockade of either hyperpolarization-activated cyclic nucleotide-gated (HCN) or muscarine-sensitive (M) channels increased impedance frequency variation and delay between membrane current (I_m) and potential (V_m). *A*: example chirp currents (*top*) and V_m responses (*bottom*) before (*left*, black) and after (*right*, red) ZD7288 application. Data from 9 recordings at 36 steady-state membrane potential (V_{ss}) values from 6 animals. *B*: after block of HCN channels with ZD7288, input impedance (Z_{IN}) increased 2-fold at low frequencies. Population average impedance (across animals and V_{ss}) is shown as mean ± SE (solid line and shaded region). The gray line is the difference between the averages. *C*: impedance phase decreased at all frequencies after HCN blockade, reducing I_m-V_m synchrony. *D*: example chirp currents (*top*) and responses (*bottom*) before (*left*) and after (*right*) XE991 application. Data include 6 recordings at 14 V_{ss} values from 6 animals. *E*: after block of M channels with XE991, a large increase in low-frequency Z_{IN} was seen with peak at 3.5 Hz. Arrowheads indicate resonant frequencies. *F*: after M channel block, impedance phase increased at low frequencies (<2 Hz) but decreased at higher frequencies. *G*: the increased low-frequency impedance after blockade of HCN or M channels produced higher Z_{IN} frequency variations across V_{ss}. Z_{IN} frequency variation is displayed as linear fit (solid lines) and 95% confidence intervals (dotted lines). M channel blockade increased frequency variation mainly at depolarized potentials, whereas HCN blockade had a greater effect at hyperpolarized potentials. *H*: the resonance strength, calculated as the maximum impedance amplitude divided by steady-state impedance amplitude [$|Z_{IN}(0)|$], was <1.2 for all membrane potentials under control conditions and after HCN-channel block. After M-channel block, however, a larger resonance was observed at depolarized membrane potentials. *I*: the mean absolute time lag between the input current and local membrane potential increased by ~1 ms after HCN-channel block (red) and ~2 ms after M-channel block (green). Control data (black) are the same as shown in *F*. Control data from 53 recordings at 181 V_{ss} values from 47 animals.

effect on the change in Z_{IN}, but the different branching patterns produced effects that were stronger within different frequency ranges (Fig. 6, *D* and *E*).

Compartmentalization of neurons increases the gain and synchrony between local input currents and changes in membrane potential (Häusser and Mel 2003; London and Häusser 2005). This is offset in part by lower signal transfer between cell regions. The net effect of the morphology on the membrane impedance is therefore not immediately apparent. To assess it, we thus calculated the Z_{TR} in an all-to-all manner, with current frequencies between 0 and 5 kHz injected successively into each model segment and the impedance measured in all other segments. The Z_{TR} profiles from one dendritic segment are illustrated for a 35-Hz current in Fig. 6*F*, *left* (delay) and *right* (amplitude). The segments near the current injection site had higher, whereas more distant segments had lower, Z_{TR} than an isopotential equivalent. If two synaptic inputs impinged upon the cell, one at the arrowhead, their integration would occur with greater gain and increased synchrony if the second input impinged in the brown region in Fig. 6*F*. For the first synaptic input in LGMD's field A as in the example shown, the dendritic branches of field A are within the area of improved coincidence detection and those of fields B and C are within the area of reduced coincidence detection (Fig. 1*A*).

To determine how far signals propagated before the increased attenuation overcame the increased local Z_{IN}, we quantified, for each segment, its area of increased Z_{TR} relative to an isopotential equivalent. This was recorded as the percentage of membrane for which transfer amplitudes were higher and delays shorter compared with the equivalent isopotential model. For some LGMD segments, the surface area with increased transfer amplitude was as high as 90% and amounted to ~70% for the average segment (Fig. 6*G*). Collapsing the LGMD's three dendritic fields into three electrotonically equivalent cylinders reduced this area substantially (Fig. 6*G*; see also Fig. 7*A*). The Purkinje model had an area of increased transfer similar to the LGMD, whereas models of the pyramidal and OLM neurons, had an increased transfer

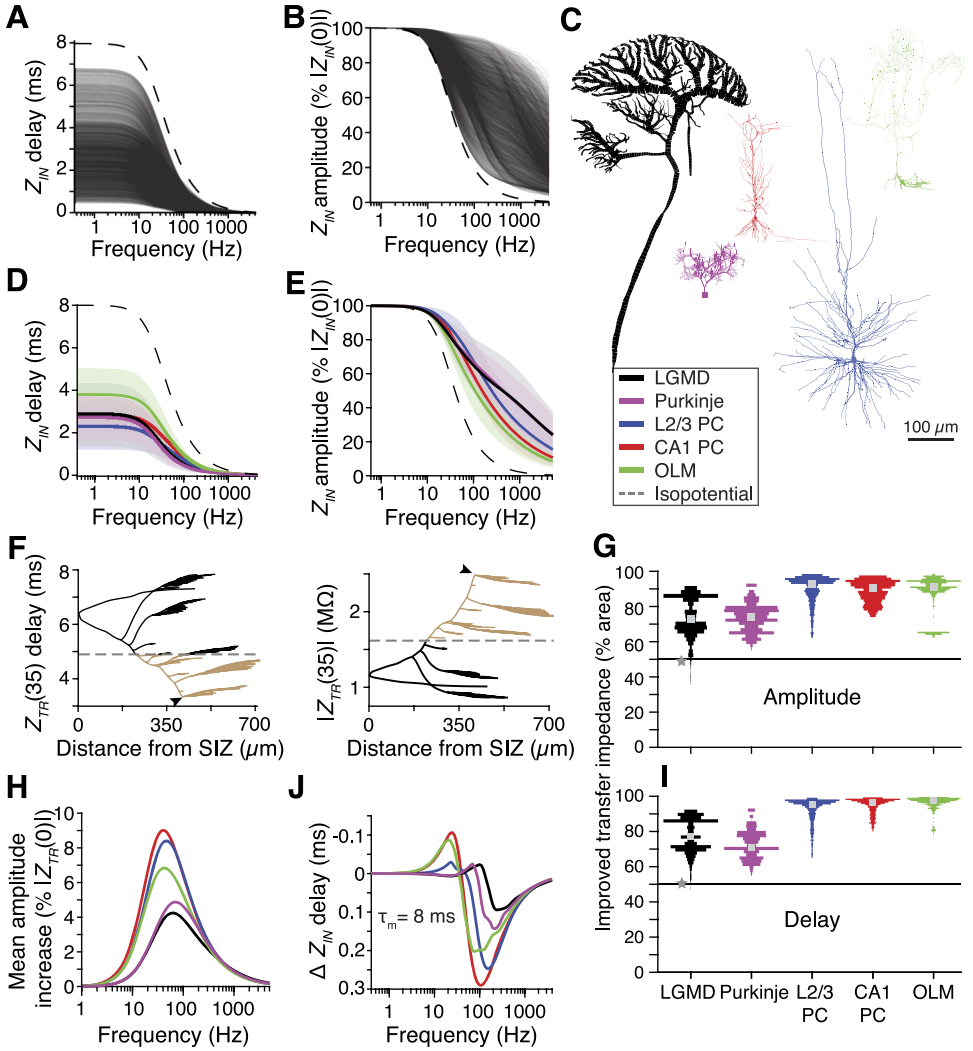

Fig. 6. Simulations of passive neurons reveal the influence of morphology on impedance characteristics. *A*: every section of the lobula giant movement detector (LGMD) model (thin black lines) had shorter input impedance (Z_{IN}) delays than an isopotential model (dashed line). *B*: all sections of the LGMD model (thin black lines) exhibited a decrease in Z_{IN} amplitude smaller than that of an isopotential model (dashed line). For each section the impedance amplitude is normalized to impedance at 0 Hz [$|Z_{IN}(0)|$]. The difference between the Z_{IN} amplitude and that of an isopotential model was maximal at ~200 Hz. *C*: the effect of neuronal morphology on impedance was tested in the LGMD (black) and 4 other cell morphologies of different size and shape: a cerebellar Purkinje cell (purple), a hippocampal CA1 pyramidal cell (PC) (red), a cortical layer 2/3 pyramidal cell (blue), and a CA1 oriens-lacunosum/moleculare interneuron (OLM; green). *D*: all neuron models tested had large decreases in input delay compared with an isopotential equivalent model. Data are color coded as in *C* and presented as means ± SD (solid lines and shaded regions). *E*: all morphologies had more consistent Z_{IN} amplitude relative to their isopotential equivalents, with lower frequency variation. Data presented as in *D*. *F*: data from example dendritic segments of the LGMD model show that at 35 Hz the transfer impedance (Z_{TR}) delay (*left*) increased and the amplitude (*right*) decreased with distance from the site of current injection (arrowheads). Segments for which Z_{TR} had higher amplitude or shorter delay than that of an isopotential equivalent neuron (dashed line) are brown. Data in *G* and *I* were measured by summing the surface area of brown segments and dividing by the total surface area. *G*: for each neuron model segment, we summed the surface area of other model segments for which signal transfer was increased compared with an isopotential equivalent and divided by the neuron's total surface area. Bar widths indicate how many model segments had improved transfer (higher gain and lower delay) for each percentage range, and gray squares mark the average segment. All morphologies had increased transfer amplitudes compared with an isopotential equivalent model (zero axial resistance), with the LGMD and Purkinje morphologies having improved transfer for a smaller percentage of the neuron segments. Gray stars indicate mean value for the LGMD model where the 3 dendritic fields were collapsed into 3 electrotonically equivalent cylinders. *H*: for all models, an average all-to-all Z_{TR} was measured as a function of frequency and compared to the impedance of an isopotential equivalent. The increase of each cell's mean transfer amplitude as a function of frequency from isopotential reveals a band-pass increase in average transfer gain. *I*: the percentage of membrane area with reduced transfer delay for each morphology was similar to that with an increase in transfer gain. Plotted as in *G*. *J*: the average all-to-all transfer delay from membrane current to membrane potential for each model was similar, with no difference at low frequencies, a slightly longer delay near the frequency of the cell's peak gain, and reduced delays at higher frequencies. In *G* and *I*, the black horizontal line marks the level of equal surface area with improved or reduced Z_{TR}.

amplitude from most segments to ~90% of the neuron's surface area (Fig. 6*G*).

We also calculated membrane area-weighted averages of the transfer amplitude to examine the net effect of the morphology on signal transfer. Examination of the net transfer amplitude at different frequencies showed that each morphology generated a band-pass increase in transfer amplitude (Fig. 6*H*). The CA1 pyramidal model had the highest increase, with 40-Hz inputs increasing by 9%. The LGMD and Purkinje morphologies generated smaller increases, 4–5%, shifted at higher frequencies near 65 Hz. Because branched morphologies cause membrane potentials to attenuate, it would not have been surprising

if their net effect were a reduced transfer amplitude relative to an isopotential model, but this was not the case.

For all morphologies, the reduction in input delay was partially offset by the increase in transfer delay. The improved timing of the Z_{IN} spread throughout most of the neurons, and the lower transfer delay propagated to almost the same membrane area as did the increased transfer amplitude (Fig. 6*I*). To calculate the total transfer delay, values were weighted by the strength of the transfer amplitude: if there is minimal signal transfer between two segments, then the timing of that transfer is less relevant. The net impact of morphology on the average transfer delay was small (≤0.3 ms for all frequencies; Fig. 6*J*). All realistic morphologies had slightly smaller net transfer delays than an isopotential equivalent model for signals above 100 Hz. The amount and frequency range of this improvement scaled with the τ_m used for simulations: simulations with τ_m = 16 ms had twice the improvement in delay, with a peak improvement at lower frequencies. The overall effect was minimal on low-frequency signals but could improve the timing of high-frequency signals, like those generated from fast synaptic currents.

To test whether the described properties are unique to realistic morphologies, we performed the same calculation for simpler morphologies including unbranched cables and Rall branching models (schematically illustrated in Fig. 7, *A*, *bottom*, and *B*; MATERIALS AND METHODS). Neither the Rall branching model (illustrated in Supplemental Fig. S3) nor a uniform 10-μm cable produced the band-pass increase in net gain found for the realistic morphologies (Fig. 7*A*). We also tested an LGMD morphology with each dendritic field collapsed into an electrotonically equivalent cable, which maintained a mean transfer amplitude similar to the full morphology (Fig. 7*A*). This suggested that it was the electrotonic structure and not the branching pattern that determined the net transfer amplitude, so we "pinched" the branch points of the Rall model (as illustrated at Fig. 7*A*, *bottom*; MATERIALS AND METHODS) and found the mean transfer gain increased and almost reached the peak value seen in the LGMD model (Fig. 7*A*). To explore whether any change in electrotonic structure increased the overall transfer gain, we tested several manipulations of unbranched cable models (Fig. 7*B*). Reducing cable diameter, either uniformly or with pinches, increased the mean transfer gain of the cables, whereas uniform tapering did not. Using a cable with one or five points of reduced diameter generated net impedance gains with peaks 51% and 84%, respectively, those of the cable with 10 pinches shown in Fig. 7*B*. A cable with randomly changing diameter (20 μm average) produced an overall impedance amplitude similar to a uniform reduction to 2 μm (Fig. 7*B*). As in the realistic morphologies, the mean transfer delay was reduced as the mean transfer amplitude increased (Fig. 7, *C* and *D*). Thus all manipulations that increased axial resistance relative to membrane resistance produced increases in mean transfer amplitude and decreases in mean transfer delay.

Pronounced effect of impedance on temporal input discrimination. Blockade of g_H reduces the LGMD's ability to discriminate the spatial pattern of its synaptic inputs, and blockade of g_M reduces the LGMD's spike timing reliability (Dewell and Gabbiani 2018a, 2018b). However, the role of the LGMD's active conductances in discriminating temporal patterns has not been addressed.

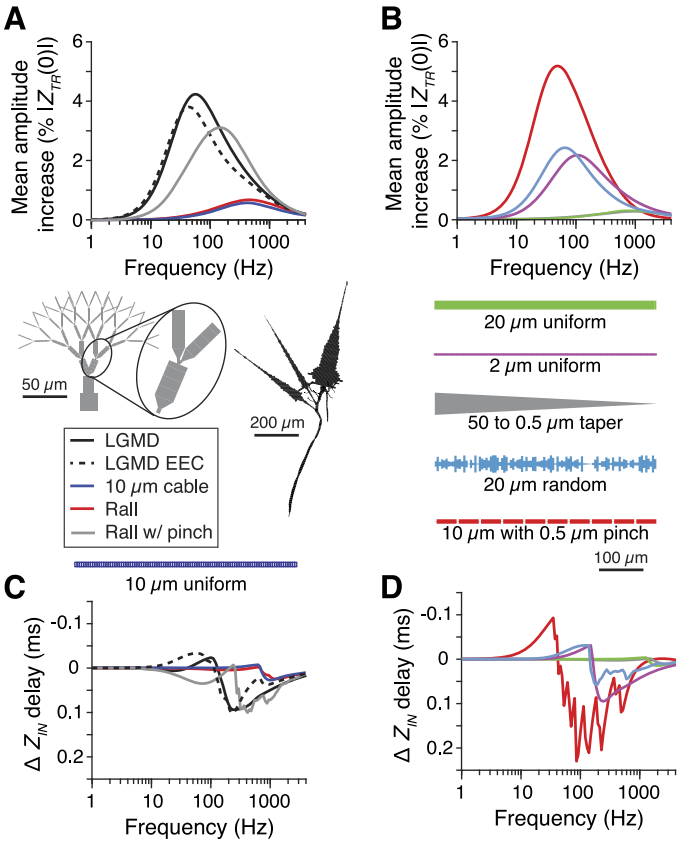

Fig. 7. Simplified morphology simulations reveal that local reduction of axial conductance increases the net transfer impedance (Z_{TR}). *A*: the mean transfer amplitude was measured as in Fig. 6*H*, with the data from the full lobula giant movement detector (LGMD) model the same (black line). Compressing each of the LGMD's dendritic fields into an electrotonically equivalent cable (LGMD EEC, dashed line) produced little change in Z_{TR} amplitude. A 10-μm-diameter uniform cable (blue) and a Rall branching model (red) had mean transfer amplitudes within 1% of an isopotential equivalent for all frequencies. Reducing the diameter at each branch point (Rall with pinch, gray) increased the mean transfer amplitude; *inset* shows detail of pinch. *B*: mean transfer amplitude was measured for a series of unbranched cables [2 with uniform 2- and 20-μm diameters are illustrated here (magenta and green)], a tapered cable (gray), a cable with random diameters with mean of 20 μm (blue), and a 10-μm cable with 10 points pinched to 0.5 μm (red). $|Z_{TR}(0)|$, transfer impedance amplitude at 0 Hz. *C* and *D*: the mean transfer delay, plotted as in Fig. 6*J*. All manipulations that produced larger mean transfer amplitudes also produced shorter mean transfer delays.

In a full LGMD model (Dewell and Gabbiani 2018a, 2018b), 200 excitatory inputs with 25-ms jitter failed to produce spiking, but after blocking g_H and g_M a burst of spikes was produced (Fig. 8*A*). Blocking these conductances has multiple effects: an increase in the input resistance, an increase in the membrane time constant, and removal of the inductance generated by the channels. To determine the relative importance of the conductance and inductance effects, we replaced g_H and g_M by a voltage-independent conductance (leak) with or without an additional frequency-dependent conductance (inductive leak), both of which had the same resting conductance. After g_H and g_M were replaced by the leak conductance, a burst of spikes was still generated to these inputs (Fig. 8*A*). When g_H and g_M were replaced by the inductive leak, the response matched the model with the active channels. Simulations with nine different jitter levels (0–50 ms) at each of 32 different random subsets of dendritic branches showed that the full

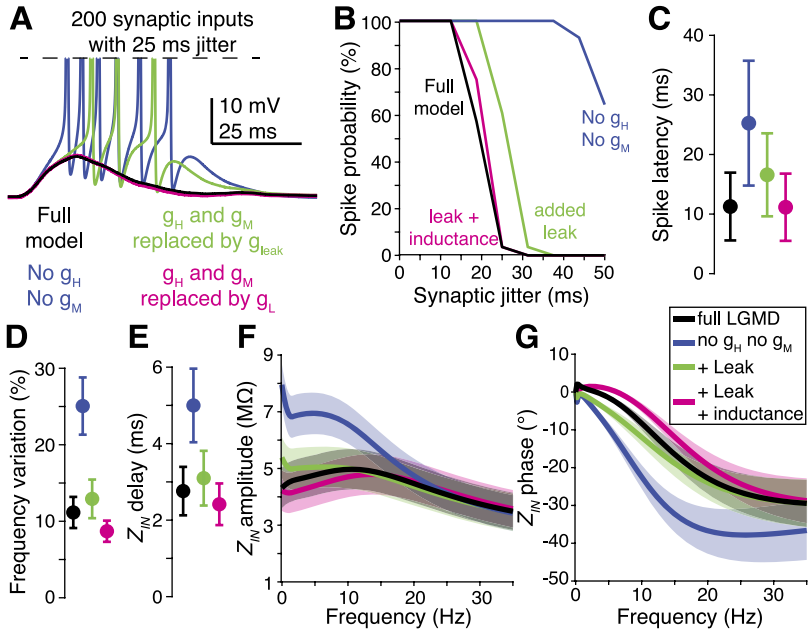

Fig. 8. Lobula giant movement detector (LGMD) model simulations show influence of hyperpolarization-activated cyclic nucleotide-gated channel-mediated (g_H) and muscarine-sensitive-channel-mediated (g_M) conductances on sensitivity to synaptic input timing and impedance profile. *A*: example traces of model responses to 200 excitatory synaptic inputs with 25-ms jitter. In the full and the leak-with-inductance (g_L) models no spike was generated. In models without g_H or g_M, or if they were replaced by a leak conductance (g_{leak}) a burst of spikes was generated. Spikes are truncated at dashed line. *B*: in the full LGMD model (black) synchronous inputs reliably generated spikes, but for inputs with less reliable input timing (jitter > 20 ms) spikes were not produced. Removal of g_H and g_M (blue) reduced the timing discrimination. When the active conductances were replaced by a leak conductance the selectivity was partially restored (green). Replacing g_H and g_M with an inductive leak (magenta; see MATERIALS AND METHODS) fully restored the sensitivity to synaptic timing. *C*: the full LGMD model generated spikes with a short latency after the inputs began. After g_H and g_M blockade spikes occurred later and with less reliable timing. Restoration of the conductance (green) and inductance (magenta) both reduced spike latency and timing variability. *D* and *E*: the frequency variation and mean absolute delay from membrane current to membrane potential of the full model (at −65 mV) matched that of LGMD experimental data (cf. Figs. 3*E* and 4*G*) and were both increased by the removal of g_H and g_M. Z_{IN}, input impedance. *F* and *G*: the impedance amplitude and phase profiles (at −65 mV) for the full model were similar to experimental data (cf. Figs. 3*A* and 4*A*). The effects of blocking g_H and g_M were qualitatively similar to experimental data, but the changes were of smaller magnitude (cf. Fig. 5). For *C*–*G*, error bars and shaded regions are ± 1 SD. For *C* variability was measured across trials. For *D*–*G*, the variability was measured across different model sections corresponding to the same region of dendritic field A as the experimental recordings.

model was the most sensitive to the input synchrony. Removal of g_H and g_M greatly reduced this sensitivity, replacing g_H and g_M with a leak restored much of it, and replacement with an inductive leak fully restored it (Fig. 8*B*). These changes in spike probability were accompanied by similar effects on spike timing. Removal of g_H and g_M also increased the spike latency (measured from the start of synaptic excitation) as well as its variability, but this too was partly restored by the leak conductance and fully by the inductive leak (Fig. 8*C*). In additional simulations we removed g_H and g_M separately and found that g_M had a larger effect on sensitivity to input synchrony. After g_H block sensitivity to input synchrony decreased by 5 ms, whereas g_M block reduced sensitivity to input synchrony by 20 ms (Supplemental Fig. S4; https://doi.org/10.5281/zenodo.2635834). This matches previous experimental findings on the role of g_M in the LGMD's spike timing precision (Dewell and Gabbiani 2018b).

We then examined the impedance properties of model sections corresponding to the dendritic region used in experimental recordings. For the different models the frequency variation (Fig. 8*D*) and mean Z_{IN} delay (Fig. 8*E*) were good indicators of each model's timing sensitivity. The impedance amplitude profiles (Fig. 8*F*) reveal that the changes in frequency variation were produced by a decreased low-frequency impedance amplitude caused by both the conductance and inductance (whether generated by g_H and g_M or the inductive leak). The leak conductance increased the impedance phase at higher frequencies, and the inductance increased it at lower frequencies (Fig. 8*G*).

To test that these properties are not unique to the LGMD model, we replicated the same simulations using 100 synaptic inputs impinging with varying degrees of synchrony onto the Rall model neuron (Supplemental Fig. S3). In this model as well, addition of g_H and g_M or a voltage-independent inductance produced qualitatively similar changes to the impedance profile and increased the model's ability to discriminate the temporal synchrony of excitatory inputs (Supplemental Fig. S3).

DISCUSSION

Here we have described the impedance properties of the LGMD in vivo, measured over the range of frequencies encompassing most of the signal power mediated by its synaptic inputs. We found that the membrane impedance amplitude is consistent over the range of subthreshold membrane potentials and input frequencies involved in the detection of approaching objects. Furthermore, the membrane impedance revealed small delays between input current and changes in membrane potential. This consistency was shaped by the conductances g_H and g_M, as well as the neuron's branching morphology and electrotonic compartmentalization. Modeling revealed that this increases the LGMD's ability to discriminate temporal patterns of excitatory synaptic inputs.

Despite a high rate of spontaneous and stimulus-evoked synaptic inputs, most of the LGMD's V_m power was concentrated at low frequencies (Fig. 1, *C* and *F*). During looming stimuli, as the rate of excitation increased, the dominant signal frequency actually decreased, with >50% of the V_m spectral power below 1.5 Hz. As neither the Z_{IN} nor the Z_{TR} amplitude was low pass (Fig. 3*A*), this must reflect the characteristics of presynaptic inputs to the LGMD. Neither the membrane gain nor the delay between I_m and V_m changed dramatically over the frequencies tested, favoring integration over a broad frequency range during looming.

To determine what shapes the frequency dependence of the impedance gain, we used pharmacological manipulations and computational modeling. We found that the neuron's morphology and the active conductances g_H and g_M (Fig. 5*G*) dramatically reduced frequency variation of the impedance gain, making the LGMD membrane impedance more broadband. This was surprising, because both g_H and g_M usually make neurons more band pass (Hönigsperger et al. 2015; Hu et al. 2009; Hutcheon and Yarom 2000; Narayanan and Johnston 2008). The primary effect of g_H on the membrane impedance (Fig. 5, *B* and *C*) is actually the same as in other neurons: a reduction of low-pass filtering and impedance delay. Whether g_H narrows the membrane band-pass properties or broadens them, as it does here and in CA3 interneurons (Anderson et al. 2011), depends on the relative balance of its effects and those of other membrane properties.

In addition to showing low frequency variation and delays between I_m and V_m, the impedance of the LGMD also showed consistency across holding potentials. As an object approaches the eye, increasing excitation causes dendritic depolarization of >20 mV, so changes in dendritic integration properties with V_m would influence the detection of impending collisions. The Z_{IN} and Z_{TR} profile remained consistent from −70 to −55 mV (Fig. 4, *D* and *E*). This consistency can also be largely explained by g_H and g_M. At hyperpolarized potentials g_H increases, dominating the membrane conductance. Conversely, g_M increases with depolarization. At the LGMD's resting membrane potential (−65 mV), both channels have large conductances and shallow activation kinetics (Dewell and Gabbiani 2018a, 2018b). If the activation ranges of g_H and g_M had less overlap, the impedance profile would be less consistent across membrane potentials and the channels would be more likely to create separate hyperpolarized and depolarized resonances as seen in pyramidal cells (Hu et al. 2002, 2009).

Synaptic integration is influenced by the input timing as well as its gain. We found that the LGMD exhibited shorter delays between I_m and V_m than could be explained by an electrical circuit model (Fig. 4*G*, Supplemental Fig. S2*E*). These delays were reduced by both g_H and g_M (Fig. 5*I*). On average, blockade of g_M produced a larger increase in delays than g_H blockade, except at frequencies near the peak membrane power during looming stimuli (~1.3 Hz; Fig. 1*F*). The influence of g_H at low frequencies is consistent with its effect on synaptic pattern discrimination during looming, which occurs only with prolonged periods of excitation (Dewell and Gabbiani 2018a). In contrast, the ability to discriminate the timing of simulated synaptic inputs was greatly reduced by removal of g_M from the LGMD model (Fig. 8, Supplemental Fig. S4), a feature that would be difficult to test experimentally because the g_M blocker XE991 also has presynaptic effects (Dewell and Gabbiani 2018b). That the LGMD V_m exhibits an impedance phase/delay of 0 near 1 Hz contrasts with its spiking, which has a phase/delay = 0 near 6 Hz (Dewell and Gabbiani 2018b). The reason for this discrepancy is not obvious. Modeling studies have found that stimulation with low-amplitude sinusoidal currents and moderate noise levels produce the sub- and suprathreshold phases nearest zero at the same input frequency (Richardson et al. 2003; Rotstein 2017b). However, experimental data from hypoglossal motor neurons have also found spiking phases near 0 at higher frequency than the subthreshold membrane potential (van Brederode and Berger 2008, 2011).

Although g_H and g_M decreased I_m-V_m delays, the delays remained lower after their blockade than those of an equivalent circuit model. Testing a realistic LGMD model revealed that morphology influenced the membrane's Z_{IN} as much as active conductances by compartmentalizing the neuron (Fig. 6, *A* and *B*). This led to increased input gain and reduced input delays compared with the corresponding isopotential model with zero axial resistivity. Previous modeling of pyramidal and Purkinje neurons has also found that dendritic branches reduce low-pass filtering (Dhupia et al. 2015; Ostojic et al. 2015). This led us to wonder how the influence of LGMD's morphology on impedance compared to other cell morphologies, and whether the increase in input impedance caused by an extended neuronal morphology was counteracted by decreased signal propagation. We tested this with transfer impedance simulations of five realistic neuronal morphologies and found the result to hold across all of them.

In neurons, in vivo synaptic currents impinge throughout the dendrites and continuously integrate with new inputs. We thus measured all-to-all impedance transfer rather than transfer from individual dendrites to the site of spike initiation. As far as we know, this is the first examination of the sum transfer of a dendritic arbor. It revealed that in the LGMD, as well as other cells, the net effect of morphology is an increase in all-to-all impedance gain and a decrease in high-frequency delay between I_m and V_m. Additionally, we found that the net increase in gain is highest between 30 and 100 Hz (Fig. 6*H*). Although their magnitudes were consistent, the frequency range of these changes depended on the simulated membrane time constant. By testing simpler morphologies, we found that uniform cables and Rall branching models exhibit smaller increases in mean transfer amplitude that grew when introducing local nonuniformities in cable diameter (Fig. 7, *A* and *B*). Each manipulation that increased voltage compartmentalization (increasing axial resistance relative to membrane resistance) produced overall increases to the transfer amplitude and reductions of the transfer delay. This is explained by the lack of high-frequency attenuation of axial resistance, so that extended morphologies with larger axial relative to membrane resistance produce less low-pass filtering and increased impedance for high-frequency inputs. These simulations expand upon previous findings on the effects of dendritic morphology on a neuron's integration capabilities (Dhupia et al. 2015; Mainen and Sejnowski 1996; Moore et al. 1988).

Ultimately, the integration properties of a neuron are dictated by the pattern of its inputs and its computational role. For hippocampal pyramidal neurons that receive theta rhythmic inputs, a strong theta (4–10 Hz) resonance and synchrony could be advantageous (Hu et al. 2009; Hutcheon and Yarom 2000; Vaidya and Johnston 2013). Similarly, it might be a

computational benefit for cortical neurons to exhibit large impedance changes with membrane potential to enhance differences between up and down network states (Gutfreund et al. 1995; Hasselmo 2005; Heys et al. 2010; Wang 2010). For auditory neurons, specialized in detecting high-frequency sound waves, a fast membrane time constant and high-frequency inductance lead to broadband membrane impedances with resonance at frequencies up to 400 Hz (Mikiel-Hunter et al. 2016; Remme et al. 2014). The LGMD detects approaching objects and discriminates their specific input patterns from many others over a wide range of membrane potentials over timescales ranging from milliseconds to tens of milliseconds (Jones and Gabbiani 2010) as well as over several seconds (Dewell and Gabbiani 2018a). Thus achieving broadband membrane impedance for corresponding ranges of input frequencies and membrane potentials by a balance of active membrane conductances and an extended morphology is exactly what is needed to fine-tune escape behaviors.

GRANTS

This research was funded by grants from the National Institute of Mental Health (MH-065339), National Science Foundation (NSF) Division of Mathematical Sciences (DMS-1120952), and NSF Division of Information and Intelligent Systems (IIS-1607518).

DISCLOSURES

No conflicts of interest, financial or otherwise, are declared by the authors.

AUTHOR CONTRIBUTIONS

R.B.D. and F.G. conceived and designed research; R.B.D. performed experiments; R.B.D. analyzed data; R.B.D. and F.G. interpreted results of experiments; R.B.D. and F.G. prepared figures; R.B.D. and F.G. drafted manuscript; R.B.D. and F.G. edited and revised manuscript; R.B.D. and F.G. approved final version of manuscript.

ENDNOTE

At the request of the authors, readers are herein alerted to the fact that additional materials related to this manuscript may be found at https://senselab.med.yale.edu/ModelDB. These materials are not a part of this manuscript, and have not undergone peer review by the American Physiological Society (APS). APS and the journal editors take no responsibility for these materials, for the website address, or for any links to or from it.

REFERENCES

Anderson WD, Galván EJ, Mauna JC, Thiels E, Barrionuevo G. Properties and functional implications of I_h in hippocampal area CA3 interneurons. *Pflugers Arch* 462: 895–912, 2011. doi:10.1007/s00424-011-1025-3.

Barrow AJ, Wu SM. Low-conductance HCN1 ion channels augment the frequency response of rod and cone photoreceptors. *J Neurosci* 29: 5841–5853, 2009. doi:10.1523/JNEUROSCI.5746-08.2009.

Branco T, Clark BA, Häusser M. Dendritic discrimination of temporal input sequences in cortical neurons. *Science* 329: 1671–1675, 2010. doi:10.1126/science.1189664.

Branco T, Häusser M. Synaptic integration gradients in single cortical pyramidal cell dendrites. *Neuron* 69: 885–892, 2011. doi:10.1016/j.neuron.2011.02.006.

Cole KS. Rectification and inductance in the squid giant axon. *J Gen Physiol* 25: 29–51, 1941. doi:10.1085/jgp.25.1.29.

Cuntz H, Borst A, Segev I. Optimization principles of dendritic structure. *Theor Biol Med Model* 4: 21, 2007. doi:10.1186/1742-4682-4-21.

Das A, Rathour RK, Narayanan R. Strings on a violin: location dependence of frequency tuning in active dendrites. *Front Cell Neurosci* 11: 72, 2017. doi:10.3389/fncel.2017.00072.

Delmas P, Brown DA. Pathways modulating neural KCNQ/M (Kv7) potassium channels. *Nat Rev Neurosci* 6: 850–862, 2005. doi:10.1038/nrn1785.

Dembrow NC, Zemelman BV, Johnston D. Temporal dynamics of L5 dendrites in medial prefrontal cortex regulate integration versus coincidence detection of afferent inputs. *J Neurosci* 35: 4501–4514, 2015. doi:10.1523/JNEUROSCI.4673-14.2015.

Dewell RB, Gabbiani F. Biophysics of object segmentation in a collision-detecting neuron. *eLife* 7: e34238, 2018a. doi:10.7554/eLife.34238.

Dewell RB, Gabbiani F. M current regulates firing mode and spike reliability in a collision-detecting neuron. *J Neurophysiol* 120: 1753–1764, 2018b. doi:10.1152/jn.00363.2018.

Dhupia N, Rathour RK, Narayanan R. Dendritic atrophy constricts functional maps in resonance and impedance properties of hippocampal model neurons. *Front Cell Neurosci* 8: 456, 2015. doi:10.3389/fncel.2014.00456.

Erchova I, Kreck G, Heinemann U, Herz AV. Dynamics of rat entorhinal cortex layer II and III cells: characteristics of membrane potential resonance at rest predict oscillation properties near threshold. *J Physiol* 560: 89–110, 2004. doi:10.1113/jphysiol.2004.069930.

Eyal G, Verhoog MB, Testa-Silva G, Deitcher Y, Lodder JC, Benavides-Piccione R, Morales J, DeFelipe J, de Kock CP, Mansvelder HD, Segev I. Unique membrane properties and enhanced signal processing in human neocortical neurons. *eLife* 5: e16553, 2016. doi:10.7554/eLife.16553.

Fotowat H, Harrison RR, Gabbiani F. Multiplexing of motor information in the discharge of a collision detecting neuron during escape behaviors. *Neuron* 69: 147–158, 2011. doi:10.1016/j.neuron.2010.12.007.

Gabbiani F, Krapp HG. Spike-frequency adaptation and intrinsic properties of an identified, looming-sensitive neuron. *J Neurophysiol* 96: 2951–2962, 2006. doi:10.1152/jn.00075.2006.

Gabbiani F, Krapp HG, Koch C, Laurent G. Multiplicative computation in a visual neuron sensitive to looming. *Nature* 420: 320–324, 2002. doi:10.1038/nature01190.

Gabbiani F, Mo C, Laurent G. Invariance of angular threshold computation in a wide-field looming-sensitive neuron. *J Neurosci* 21: 314–329, 2001. doi:10.1523/JNEUROSCI.21-01-00314.2001.

Gastrein P, Campanac E, Gasselin C, Cudmore RH, Bialowas A, Carlier E, Fronzaroli-Molinieres L, Ankri N, Debanne D. The role of hyperpolarization-activated cationic current in spike-time precision and intrinsic resonance in cortical neurons in vitro. *J Physiol* 589: 3753–3773, 2011. doi:10.1113/jphysiol.2011.209148.

Gray JR, Lee JK, Robertson RM. Activity of descending contralateral movement detector neurons and collision avoidance behaviour in response to head-on visual stimuli in locusts. *J Comp Physiol A Neuroethol Sens Neural Behav Physiol* 187: 115–129, 2001. doi:10.1007/s003590100182.

Gutfreund Y, Yarom Y, Segev I. Subthreshold oscillations and resonant frequency in guinea-pig cortical neurons: physiology and modelling. *J Physiol* 483: 621–640, 1995. doi:10.1113/jphysiol.1995.sp020611.

Hasselmo ME. What is the function of hippocampal theta rhythm?—linking behavioral data to phasic properties of field potential and unit recording data. *Hippocampus* 15: 936–949, 2005. doi:10.1002/hipo.20116.

Häusser M, Mel B. Dendrites: bug or feature? *Curr Opin Neurobiol* 13: 372–383, 2003. doi:10.1016/S0959-4388(03)00075-8.

Heys JG, Giocomo LM, Hasselmo ME. Cholinergic modulation of the resonance properties of stellate cells in layer II of medial entorhinal cortex. *J Neurophysiol* 104: 258–270, 2010. doi:10.1152/jn.00492.2009.

Holmes WR, Segev I, Rall W. Interpretation of time constant and electrotonic length estimates in multicylinder or branched neuronal structures. *J Neurophysiol* 68: 1401–1420, 1992. doi:10.1152/jn.1992.68.4.1401.

Hönigsperger C, Marosi M, Murphy R, Storm JF. Dorsoventral differences in Kv7/M-current and its impact on resonance, temporal summation and excitability in rat hippocampal pyramidal cells. *J Physiol* 593: 1551–1580, 2015. doi:10.1113/jphysiol.2014.280826.

Horowitz P, Hill W. *The Art of Electronics*. Cambridge, UK: Cambridge University Press, 2015.

Hu H, Vervaeke K, Graham LJ, Storm JF. Complementary theta resonance filtering by two spatially segregated mechanisms in CA1 hippocampal pyramidal neurons. *J Neurosci* 29: 14472–14483, 2009. doi:10.1523/JNEUROSCI.0187-09.2009.

Hu H, Vervaeke K, Storm JF. Two forms of electrical resonance at theta frequencies, generated by M-current, h-current and persistent Na^+ current in rat hippocampal pyramidal cells. *J Physiol* 545: 783–805, 2002. doi:10.1113/jphysiol.2002.029249.

Hutcheon B, Miura RM, Puil E. Subthreshold membrane resonance in neocortical neurons. *J Neurophysiol* 76: 683–697, 1996. doi:10.1152/jn.1996.76.2.683.

Hutcheon B, Yarom Y. Resonance, oscillation and the intrinsic frequency preferences of neurons. *Trends Neurosci* 23: 216–222, 2000. doi:10.1016/S0166-2236(00)01547-2.

Jaffe DB, Carnevale NT. Passive normalization of synaptic integration influenced by dendritic architecture. *J Neurophysiol* 82: 3268–3285, 1999. doi:10.1152/jn.1999.82.6.3268.

Jones PW, Gabbiani F. Synchronized neural input shapes stimulus selectivity in a collision-detecting neuron. *Curr Biol* 20: 2052–2057, 2010. doi:10.1016/j.cub.2010.10.025.

Jones PW, Gabbiani F. Impact of neural noise on a sensory-motor pathway signaling impending collision. *J Neurophysiol* 107: 1067–1079, 2012. doi:10.1152/jn.00607.2011.

Koch C. Cable theory in neurons with active, linearized membranes. *Biol Cybern* 50: 15–33, 1984. doi:10.1007/BF00317936.

London M, Häusser M. Dendritic computation. *Annu Rev Neurosci* 28: 503–532, 2005. doi:10.1146/annurev.neuro.28.061604.135703.

Mainen ZF, Sejnowski TJ. Influence of dendritic structure on firing pattern in model neocortical neurons. *Nature* 382: 363–366, 1996. doi:10.1038/382363a0.

Mauro A. Anomalous impedance, a phenomenological property of time-variant resistance. An analytic review. *Biophys J* 1: 353–372, 1961. doi:10.1016/S0006-3495(61)86894-X.

Mauro A, Conti F, Dodge F, Schor R. Subthreshold behavior and phenomenological impedance of the squid giant axon. *J Gen Physiol* 55: 497–523, 1970. doi:10.1085/jgp.55.4.497.

McGinley MJ, Liberman MC, Bal R, Oertel D. Generating synchrony from the asynchronous: compensation for cochlear traveling wave delays by the dendrites of individual brainstem neurons. *J Neurosci* 32: 9301–9311, 2012. doi:10.1523/JNEUROSCI.0272-12.2012.

McMillan GA, Gray JR. Burst firing in a motion-sensitive neural pathway correlates with expansion properties of looming objects that evoke avoidance behaviors. *Front Integr Neurosci* 9: 60, 2015. doi:10.3389/fnint.2015.00060.

Migliore M, Messineo L, Ferrante M. Dendritic I_h selectively blocks temporal summation of unsynchronized distal inputs in CA1 pyramidal neurons. *J Comput Neurosci* 16: 5–13, 2004. doi:10.1023/B:JCNS.0000004837.81595.b0.

Mikiel-Hunter J, Kotak V, Rinzel J. High-frequency resonance in the gerbil medial superior olive. *PLoS Comput Biol* 12: e1005166, 2016. doi:10.1371/journal.pcbi.1005166.

Miyasho T, Takagi H, Suzuki H, Watanabe S, Inoue M, Kudo Y, Miyakawa H. Low-threshold potassium channels and a low-threshold calcium channel regulate Ca^{2+} spike firing in the dendrites of cerebellar Purkinje neurons: a modeling study. *Brain Res* 891: 106–115, 2001. doi:10.1016/S0006-8993(00)03206-6.

Moore LE, Yoshii K, Christensen BN. Transfer impedances between different regions of branched excitable cells. *J Neurophysiol* 59: 689–705, 1988. doi:10.1152/jn.1988.59.3.689.

Narayanan R, Johnston D. The h channel mediates location dependence and plasticity of intrinsic phase response in rat hippocampal neurons. *J Neurosci* 28: 5846–5860, 2008. doi:10.1523/JNEUROSCI.0835-08.2008.

O'Shea M, Williams JL. The anatomy and output connection of a locust visual interneurone; the lobular giant movement detector (LGMD) neurone. *J Comp Physiol* 91: 257–266, 1974. doi:10.1007/BF00698057.

Ostojic S, Szapiro G, Schwartz E, Barbour B, Brunel N, Hakim V. Neuronal morphology generates high-frequency firing resonance. *J Neurosci* 35: 7056–7068, 2015. doi:10.1523/JNEUROSCI.3924-14.2015.

Peron S, Gabbiani F. Spike frequency adaptation mediates looming stimulus selectivity in a collision-detecting neuron. *Nat Neurosci* 12: 318–326, 2009. doi:10.1038/nn.2259.

Peron SP, Krapp HG, Gabbiani F. Influence of electrotonic structure and synaptic mapping on the receptive field properties of a collision-detecting neuron. *J Neurophysiol* 97: 159–177, 2007. doi:10.1152/jn.00660.2006.

Rall W. Theoretical significance of dendritic trees for neuronal input-output relations. In: *Neural Theory Modeling*, edited by Reiss RF. Palo Alto, CA: Stanford University Press, 1964, p. 73–97.

Remme MW, Donato R, Mikiel-Hunter J, Ballestero JA, Foster S, Rinzel J, McAlpine D. Subthreshold resonance properties contribute to the efficient coding of auditory spatial cues. *Proc Natl Acad Sci USA* 111: E2339–E2348, 2014. doi:10.1073/pnas.1316216111.

Richardson MJ, Brunel N, Hakim V. From subthreshold to firing-rate resonance. *J Neurophysiol* 89: 2538–2554, 2003. doi:10.1152/jn.00955.2002.

Rind FC, Simmons PJ. Orthopteran DCMD neuron: a reevaluation of responses to moving objects. I. Selective responses to approaching objects. *J Neurophysiol* 68: 1654–1666, 1992. doi:10.1152/jn.1992.68.5.1654.

Rind FC, Wernitznig S, Pölt P, Zankel A, Gütl D, Sztarker J, Leitinger G. Two identified looming detectors in the locust: ubiquitous lateral connections among their inputs contribute to selective responses to looming objects. *Sci Rep* 6: 35525, 2016. doi:10.1038/srep35525.

Rotstein HG. Resonance modulation, annihilation and generation of anti-resonance and anti-phasonance in 3D neuronal systems: interplay of resonant and amplifying currents with slow dynamics. *J Comput Neurosci* 43: 35–63, 2017a. doi:10.1007/s10827-017-0646-8.

Rotstein HG. Spiking resonances in models with the same slow resonant and fast amplifying currents but different subthreshold dynamic properties. *J Comput Neurosci* 43: 243–271, 2017b. doi:10.1007/s10827-017-0661-9.

Rotstein HG, Nadim F. Frequency preference in two-dimensional neural models: a linear analysis of the interaction between resonant and amplifying currents. *J Comput Neurosci* 37: 9–28, 2014. doi:10.1007/s10827-013-0483-3.

Schlotterer GR. Response of the locust descending movement detector neuron to rapidly approaching and withdrawing visual stimuli. *Can J Zool* 55: 1372–1376, 1977. doi:10.1139/z77-179.

Sekulić V, Chen TC, Lawrence JJ, Skinner FK. Dendritic distributions of Ih channels in experimentally-derived multi-compartment models of oriens-lacunosum/moleculare (O-LM) hippocampal interneurons. *Front Synaptic Neurosci* 7: 2, 2015. doi:10.3389/fnsyn.2015.00002.

Spruston N. Pyramidal neurons: dendritic structure and synaptic integration. *Nat Rev Neurosci* 9: 206–221, 2008. doi:10.1038/nrn2286.

Ulrich D. Dendritic resonance in rat neocortical pyramidal cells. *J Neurophysiol* 87: 2753–2759, 2002. doi:10.1152/jn.2002.87.6.2753.

Vaidya SP, Johnston D. Temporal synchrony and gamma-to-theta power conversion in the dendrites of CA1 pyramidal neurons. *Nat Neurosci* 16: 1812–1820, 2013. doi:10.1038/nn.3562.

van Brederode JF, Berger AJ. Spike-firing resonance in hypoglossal motoneurons. *J Neurophysiol* 99: 2916–2928, 2008. doi:10.1152/jn.01037.2007.

van Brederode JF, Berger AJ. GAD67-GFP+ neurons in the nucleus of Roller. II. Subthreshold and firing resonance properties. *J Neurophysiol* 105: 249–278, 2011. doi:10.1152/jn.00492.2010.

Vetter P, Roth A, Häusser M. Propagation of action potentials in dendrites depends on dendritic morphology. *J Neurophysiol* 85: 926–937, 2001. doi:10.1152/jn.2001.85.2.926.

Wahl-Schott C, Biel M. HCN channels: structure, cellular regulation and physiological function. *Cell Mol Life Sci* 66: 470–494, 2009. doi:10.1007/s00018-008-8525-0.

Wang XJ. Neurophysiological and computational principles of cortical rhythms in cognition. *Physiol Rev* 90: 1195–1268, 2010. doi:10.1152/physrev.00035.2008.

Zhu Y, Gabbiani F. Fine and distributed subcellular retinotopy of excitatory inputs to the dendritic tree of a collision-detecting neuron. *J Neurophysiol* 115: 3101–3112, 2016. doi:10.1152/jn.00044.2016.